國立臺灣大學理學院物理學系

碩士論文

Department of Physics

College of Science

National Taiwan University

Master's Thesis

早期宇宙恆星形成雲氣之物理特性

Physical Properties of the Primordial Star-Forming Cloud

何孟遠

Meng-Yuan Ho

指導教授: 吳柏鋒 博士

Advisor: Po-Feng Wu, Ph.D.

共同指導教授: 陳科榮 博士

Co-Advisor: Ke-Jung Chen, Ph.D.

中華民國 113 年 7 月

July, 2024

doi:10.6342/NTU202401221

doi:10.6342/NTU202401221

國立臺灣大學碩士學位論文

口試委員會審定書

MASTER'S THESIS ACCEPTANCE CERTIFICATE
NATIONAL TAIWAN UNIVERSITY

早期宇宙恆星形成雲氣之物理特性

Physical Properties of the Primordial Star-Forming Cloud

本論文係__何孟遠__(姓名)__R11222007__（學號）在國立臺灣大學_物理學系__(系/所/學位學程)完成之碩士學位論文，於民國 113 年 07 月 08 日承下列考試委員審查通過及口試及格，特此證明。

The undersigned, appointed by the Department / Institute of ____Physics_____ on _08_(date)_07_ (month)_2024_ (year) have examined a Master's thesis entitled above presented by_Ho Meng-Yuan___ (name)_____R11222007____ (student ID) candidate and hereby certify that it is worthy of acceptance.

口試委員 Oral examination committee:

吳翎鍾　　陳科榮　　[illegible]

(指導教授 Advisor)

胡宗珣

doi:10.6342/NTU202401221

Acknowledgements

這本碩士論文是我第一份獨立完成並撰寫成冊的研究項目。過程及內容或許仍有諸多倉促及不完備之處，但仍讓我能一窺研究的殿堂。這一路上得到許多貴人的幫助及支持，我才有機會完成這份著作，實在是感激不盡。

感謝陳科榮老師擔任我的共同指導教授，在論文題目的發想、方法論、結果上給予重大協助與指導，並且在我的大學及碩士研究生涯中不斷給予鼓勵及協助，讓我在今日仍能以天文物理研究生的身份努力著。感謝吳柏鋒老師擔任我的指導教授，在星系形成及模擬環境相關問題上給予我協助，在論文撰寫時程及目標上給予我方向。感謝黃崇源老師在模擬及分析問題上給予建議。感謝陳科榮老師、吳柏鋒老師、黃崇源老師及胡家瑜老師擔任本次論文審查的委員，將在論文審查會議上給予我專業的意見及改進的方向，讓我能成為一名更專業的天文物理研究生，為天文物理往前邁出一小步。

我也要感謝在 Ken Group 、天數館 821 研究室以及物理系以來的各個夥伴，包括松翰、柏昇、文翊及景堯學長；在研究室一起打拼的坤寶、廷軒、韋安、沛承、琮棋、彥樺及淵明；從大學部就認識的品壬、暉航、宏宇、宇寬、俊維及彥宇等等。因為有你們，我才感覺到研究不是孤身一人的奮鬥。

最後，我要感謝一路支持我的家人們，讓我在追求學業的過程中都能自主做出決定，並且時刻以我為榮。作為你們的孩子，我感到萬分榮幸。

doi:10.6342/NTU202401221

doi:10.6342/NTU202401221

摘要

紊流在恆星形成的過程中扮演了重要的角色，進而影響第一恆星的各種特徵。過往的模擬研究預測此類的恆星質量將大於當前所觀測到缺乏金屬成份之恆星，而其中的差異則可能是紊流所導致的。近期的研究顯示紊流將提高原始氣體雲的溫度，降低其中的恆星形成速率，並因而影響所形成恆星之質量。並且，過去的研究已顯示由吸積所造成的紊流在宇宙中是廣泛存在的。因此，於模擬之中加入驅動紊流能為我們提供寶貴的資訊。然而，該驅動紊流以及氣體雲之間的物理關係仍然處於尚未明瞭的狀態。

在這篇論文中，我們利用 GIZMO 進行多體的宇宙學流體模擬。同時，我們在模擬之中加入許多重要的物理機制，例如原始氣體雲的輻射冷卻機制及紊流的擴散。我們從 IllustrisTNG 計畫中的 TNG50-1 模擬，截取其中質量為 10^7 個太陽質量的迷你暗物質暈作為模擬的初始條件。藉由粒子切割的技術，我們在模擬中達到每個氣體粒子具有 0.1 個太陽質量的解析度。如此高的解析度將能使我們解析高密度氣體雲中的微小結構。在模擬完成後，我們對所有的模型進行數個物理量的分析，例如密度分佈、柯爾莫哥洛夫能量頻譜，以及紊流的馬赫數。我們發現紊流將在 1 kpc 的尺度開始形成，並在密度為 $\sim 2.78 \times 10^{-22}$ g cm^{-3} 處形成 $\mathcal{M} = 2.20 \pm 1.67$ 馬赫的強度。

我們的研究旨在為使用人工紊流的宇宙學模擬提供合理的參數。藉由限制紊

doi:10.6342/NTU202401221

流強度，我們能夠進一步的找出第三星族恆星的質量範圍。未來的研究將會專注在分析模擬中產生的高密度氣體團，並試圖以此來建立或限制第三星族恆星的初始質量函數。

關鍵字：宇宙學，早期宇宙，第三星族星，迷你暗物質暈，初始紊流

doi:10.6342/NTU202401221

Abstract

Turbulence is a pivotal factor in the star formation process, influencing the characteristics of the first star. Existing simulations have predicted the formation of stars with significantly greater mass than observed in metal-poor stars, potentially attributed to the absence of turbulence. Recent studies indicate that turbulence can raise the temperature of primordial clouds, thereby reducing the star-forming rate (SFR) and impacting the mass of the earliest stars in the universe. Additionally, research has identified accretion-driven turbulence as a universal cosmic phenomenon. While implementing driven turbulence in simulations can provide valuable insights, the underlying relationship between primordial turbulence and cloud dynamics remains unclear.

We present N-body hydrodynamics (HD) cosmological simulations by utilizing the GIZMO code, which incorporates critical physics such as radiative cooling for primordial gas and turbulence diffusion. The initial conditions are derived from mini-halo within the TNG50-1 of IllustrisTNG project at $z \sim 20$, where the total mass is around 10^7 $M_\odot$. By

doi:10.6342/NTU202401221

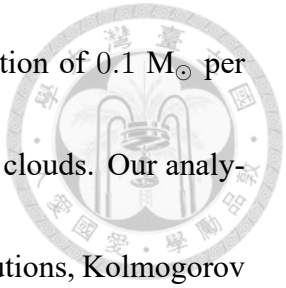

employing particle-splitting techniques, we achieve the finest resolution of 0.1 $M_\odot$ per gas particle, enabling us to unveil the intricate structure within dense clouds. Our analysis encompasses various physical properties, including density distributions, Kolmogorov spectrum, and the Mach number of the turbulence spanning the entirety of our simulations. We found out the scale of turbulence formed at the scale of ~ 1 kpc for mini-halos, and the Mach number reaches $\mathcal{M} = 2.20 \pm 1.67$ at $\sim 2.78 \times 10^{-22}$ g cm^{-3}.

This finding could be the reference for the cosmological simulations that introduced artificial-driven turbulence. By constraining the strength of turbulence, we can further constrain the mass range of Pop. III stars. Future work will focus on the analysis of gas clumps in our model, and try to build or constrain the initial mass function of Pop. III stars.

Keywords: Cosmology, Early Universe, Population III Star, Mini-halo, Primordial Turbulence

doi:10.6342/NTU202401221

Contents

doi:10.6342/NTU202401221

doi:10.6342/NTU202401221

List of Figures

doi:10.6342/NTU202401221

doi:10.6342/NTU202401221

List of Tables

doi:10.6342/NTU202401221

doi:10.6342/NTU202401221

Chapter 1 Introduction

The understanding of primordial star-forming clouds is not clear in astrophysics. Population III (Pop. III), massive and metal-free stars are often regarded as the first generation of stars. However, the cooling processes in primordial clouds are inefficient in the absence of metals, the only coolant that could cool down the primordial clouds to below 10^4 K is the molecular hydrogen (Yoshida et al., 2003). Consequently, the first-generation stars' Jeans mass is significantly higher than stars in the local universe. Also, Previous simulation studies usually assumed a spherical cloud inside a dark matter halo (Omukai, 2001, Yoshida et al., 2003). This has led to predictions that Pop. III stars have masses ranging from $50 \sim 1000$ $M_\odot$, whose mass is far larger than the usual mass of stars we can observe in the local universe (Abel et al., 1998; Omukai, 2001; Omukai & Palla, 2003; O'Shea & Norman, 2007; Hirano et al., 2014; Hosokawa et al., 2016; Klessen & Glover, 2023).

Recent studies, however, indicate that progenitors of metal-poor stars could be the candidates of Pop. III stars, have masses smaller than 100 $M_\odot$ (Umeda & Nomoto, 2005; Ishigaki et al., 2018; Skúladóttir et al., 2024; Ji et al., 2024). This discrepancy between theoretical predictions and observational data might be attributed to turbulence.

In previous simulation studies, they usually assumed a spherical well-distributed gas

doi:10.6342/NTU202401221

cloud. Such an assumption may lead to massive Pop. III stars due to the lack of turbulence and randomly distributed initial conditions. However, turbulence in primordial clouds can result in filamentary structures, forming gas clumps. Thus, Pop. III stars formed within these gas clumps might have smaller masses than initially expected (Tang & Chen, 2024).

Turbulence is typically introduced in simulations by "driving" the field, which involves applying artificial velocity dispersion in the velocity field. This method allows straightforward measurement of turbulence effects by varying the Mach numbers. However, the introduction of artificial terms can result in excess energy, potentially causing instability in simulation codes. Additionally, this method permits the application of arbitrary turbulence strengths, regardless of environmental feasibility.

The origin of the turbulence could be many. Possible sources of turbulence are from ANG feedback, stellar feedback, and gravitational accretion. In the study of the first star, we exclude any turbulence driven by stellar feedback. Also, the effect of feedback is thought to be less than the effect of turbulence in the formation of the Pop. III stars (Sharda & Menon, 2024). Hence, the dominant source of turbulence in our models is accretion-driven turbulence, and such turbulence has been confirmed as a universal process in the universe (Klessen & Hennebelle, 2010).

In this work, we propose a novel method to examine the properties of primordial gas clouds. We generate initial conditions by capturing a mini-halo within a large-scale cosmological simulation to achieve a realistic density distribution. Utilizing a particle splitting algorithm, we enhance resolution and analyze the smallest structures in our models. Our goal is to understand the strength of turbulence driven by gravitational accretion.

The structure of this paper is as follows: Chapter 2 outlines the methodology, includ-

doi:10.6342/NTU202401221

ing brief introductions to the simulation code, the selection of initial conditions, and the zoom-in method. Chapter 3 presents the evolution of our models, derived quantities, and the Mach number relation. Chapter 4 discusses the issues pertinent to our work. Finally, Chapter 5 concludes with our results and their connection to current research.

doi:10.6342/NTU202401221

doi:10.6342/NTU202401221

Chapter 2 Numerical Methodology

In this chapter, we detail the simulation processes and the underlying physics. The methodology is divided into three main stages: generating initial conditions, transforming these conditions for simulation, and analyzing the results.

1. Generating Initial Conditions: The initial conditions for our simulations are generated from the IllustrisTNG project, a large-scale cosmological simulation that provides detailed data on the structure and evolution of the universe. We extract the relevant data to capture the mini-halos in the early universe at $z \approx 20$. This ensures a more realistic starting point for our simulations.

2. Transforming Initial Conditions for GIZMO: Once the initial conditions are obtained, they are transformed into the appropriate format for the GIZMO simulation code. GIZMO is a cosmological hydrodynamic simulation tool, allowing us to achieve high resolution and accuracy in modeling the evolution of mini-halos. We perform a zoom-in simulation to focus on the detailed dynamics within a specific region of interest, enhancing the resolution and capturing small-scale structures.

doi:10.6342/NTU202401221

2.1 IllustrisTNG

The IllustrisTNG project is a state-of-the-art large-scale cosmological simulation, renowned for its detailed and comprehensive modeling of the universe. The simulation methods and details are extensively documented in two key papers (Pillepich et al., 2018; Weinberger et al., 2017). In essence, the IllustrisTNG project utilizes the moving-mesh code AREPO to conduct cosmological simulations that incorporate large-scale gravity and magnetohydrodynamics.

Among the various simulations within the IllustrisTNG project, we have selected TNG50-1 as the source of our initial conditions due to its superior resolution compared to TNG100 and TNG300. The TNG50 simulation spans a roughly 50 Mpc side length and offers the highest resolution, making it ideal for our study of mini-halos in the early universe.

Simulation Parameters	Unit	TNG50-1
Volumes	[Mpc^3]	51.7^3
L_{Box}	[Mpc/h]	35
N_{GAS}	-	2160^3
N_{DM}	-	2160^3
m_{Baryon}	[$M_\odot$/h]	8.5×10^4
m_{DM}	[$M_\odot$/h]	4.5×10^5
Cosmological Parameters	-	Planck2015
Ω_m	-	0.3089
Ω_Λ	-	0.6911
h	[100 km/s/Mpc]	0.6774

Table 2.1: Parameters of TNG50.

2.2 GIZMO

GIZMO is an advanced hydrodynamic simulation code, evolved from and serving as

doi:10.6342/NTU202401221

a descendant of GADGET-2 (Hopkins, 2015). GADGET-2 is a well-known N-body cosmological simulation code that employs smoothed-particle hydrodynamics (SPH) (Springel, 2005). In this code, gravitational forces are computed using the Tree Particle-Mesh (TreePM) algorithm, which constructs a hierarchical structure for the simulation region. The short-range gravitational forces are approximated using the multipole expansion method, which efficiently handles high spatial resolution regions, while the long-range forces are calculated using Fourier techniques, which involve computations over a limited number of grids/meshes.

Compared to other popular simulation codes, such as grid-based codes, SPH codes treat data as particles, offering advantages in angular momentum conservation. However, SPH codes face challenges like high computational costs and low-order errors. Traditional SPH codes often use artificial viscosity to handle energy dissipation, which can introduce instability and noise. Although improvements have been made in newer versions of SPH codes, issues with instabilities and low-order errors persist. On the other hand, grid-based/adaptive mesh refinement (AMR) codes address low-order errors effectively but struggle with angular momentum conservation and over-mixing issues.

GIZMO addresses these challenges by improving upon the original SPH code. In GIZMO, the kernel function discretizes the region between particles, combining the strengths of both SPH and grid-based codes. This hybrid approach allows GIZMO to achieve high-order accuracy, better fluid-mixing stability, and reduced noise. Additionally, GIZMO automatically adjusts adaptive softening lengths, preventing fluid over-mixing and preserving angular momentum conservation. Several tests have demonstrated the consistency and stability of GIZMO, making it a robust tool for cosmological simulations.

doi:10.6342/NTU202401221

By leveraging these advancements, GIZMO provides a powerful and reliable framework for investigating the complex dynamics of the early universe, particularly in the study of mini-halos and the formation of primordial stars.

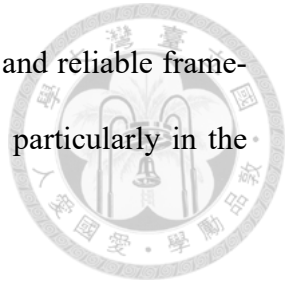

2.2.1 Meshless Equation of Motion

In GIZMO, the data is discretized into particles. For each particle, it needs to follow the conservation of energy, mass, and momentum. The Euler equation of motion can be described as (Gaburov & Nitadori, 2011):

$$\frac{\partial \mathbf{U}}{\partial t} + \nabla \cdot (\mathbf{F} - \mathbf{v}_{frame} \otimes \mathbf{U}) = 0 \tag{2.1}$$

where $\mathbf{U}$ is the state vector of conserved quantities, $\otimes$ is the outer product, and $\mathbf{v}_{frame}$ represents the velocity of the moving frame. The state vector $\mathbf{U}$ can be described as:

$$\mathbf{U} = \begin{pmatrix} \rho \\ \rho\mathbf{v} \\ \rho e \end{pmatrix} = \begin{pmatrix} \rho \\ \rho\mathbf{v} \\ \rho u + \frac{1}{2}\rho|\mathbf{v}|^2 \end{pmatrix} = \begin{pmatrix} \rho \\ \rho v_x \\ \rho v_y \\ \rho v_z \\ \rho u + \frac{1}{2}\rho|\mathbf{v}|^2 \end{pmatrix} \tag{2.2}$$

where ρ is mass density, e is the total energy, u is the internal energy, and the last operator expands the $\mathbf{v}_{frame}$ in three dimensions. The tensor $\mathbf{F}$ is the flux of conserved variables,

$$\mathbf{F} = \begin{pmatrix} \rho\mathbf{v} \\ \rho\mathbf{v} \otimes \mathbf{v} + PI \\ (\rho e + P)\mathbf{v} \end{pmatrix} \tag{2.3}$$

doi:10.6342/NTU202401221

where P is the pressure, and I is the identity tensor.

By multiplying an arbitrary Lagrangian function $\phi = \phi(\mathbf{v}, t)$ where $d\phi/dt = 0$ and integrate over the domain Ω where $d\Omega = d^{\nu}\mathbf{v}$, we can obtain:

$$0 = \int_{\Omega} \left(\frac{d\mathbf{U}}{dt}\phi + \phi\nabla \cdot (\mathbf{F} - \mathbf{v}_{frame} \otimes \mathbf{U}) \right) d\Omega \tag{2.4}$$

Apply the integration by parts of the $\phi\nabla \cdot \mathbf{F}$, we can write the above equation into:

$$0 = \int_{\Omega} \left(\frac{d\mathbf{U}}{dt}\phi - \mathbf{F} \cdot \nabla\phi \right) d\Omega + \int_{\partial\Omega} (\mathbf{F}\phi) \cdot \hat{\mathbf{n}}_{\partial\Omega} d(\partial\Omega) \tag{2.5}$$

We can eliminate the second term of the equation 2.5, which is the boundary term, by assuming the fluxes or ϕ vanishes at infinity. The equation 2.5 hence becomes:

$$0 = \frac{d}{dt} \int_{\Omega} \mathbf{U}(\mathbf{x}, t)\phi d^{\nu}\mathbf{x} - \int_{\Omega} \mathbf{F}(\mathbf{U}, \mathbf{x}, t) \cdot \nabla\phi d^{\nu}\mathbf{x} \tag{2.6}$$

In the Lagrangian code, the data is in the discretized form. As a result, we need to determine the discretization function to integrate the volume domain on particles. The function can be written in the simple form:

$$\psi_i(\mathbf{x}) = \frac{1}{\sum_j W} W(\mathbf{x} - \mathbf{x}_i, h(\mathbf{x})) \tag{2.7}$$

where W is the weighting function, also known as the kernel function.

doi:10.6342/NTU202401221

2.2.2 Kernel Functions

As the previous section mentioned, kernel functions are how the code processes the volume partition around particles.

In our model, we use the default cubic spline kernel. The 3D form of the cubic spline kernel is given by Monaghan, 1992:

$$W(\mathbf{r}, h) = \frac{8}{\pi h^3} \begin{cases} 1 - \frac{3}{2}q^2 + \frac{3}{4}q^3 & \text{if } 0 \leq \frac{r}{h} \leq 1; \\ \frac{1}{4}(2-q)^3 & \text{if } 1 \leq \frac{r}{h} \leq 2; \\ 0 & \text{otherwise} \end{cases} \tag{2.8}$$

$$\Phi_i(q, h_i) \equiv m_i \phi(q, h_i) \tag{2.9}$$

$$\phi(q, h) = \frac{2}{qh} \begin{cases} \frac{7}{5}q - \frac{2}{3}q^3 + \frac{3}{10}q^5 - \frac{1}{10}q^6 & \text{if } 0 \leq \frac{r}{h} \leq 1; \\ -\frac{1}{15} + \frac{8}{5}q - \frac{4}{3}q^3 + q^4 - \frac{3}{10}q^5 + \frac{1}{10}q^6 & \text{if } 1 \leq \frac{r}{h} \leq 2; \\ 1 & \text{otherwise} \end{cases} \tag{2.10}$$

where r is the distance to the center of the particle, h is the average smoothing length (Hsml) of the particle or the kernel size. $q = \frac{r}{2h}$ represents the ratio between r and h.

2.2.3 Meshless-Finite-Mass/Volume Hydrodynamics Solver

The major improvement of GIZMO lies in its use of finite-volume Godunov methods in the hydrodynamics solver. The new methods, Meshless-Finite-Volume (MFV) and Meshless-Finite-Mass (MFM) represent a significant advancement over traditional SPH techniques. Figure 2.1 from Hopkins (2015) illustrates the differences between MFM/MFV, mesh-based methods, and SPH methods.

doi:10.6342/NTU202401221

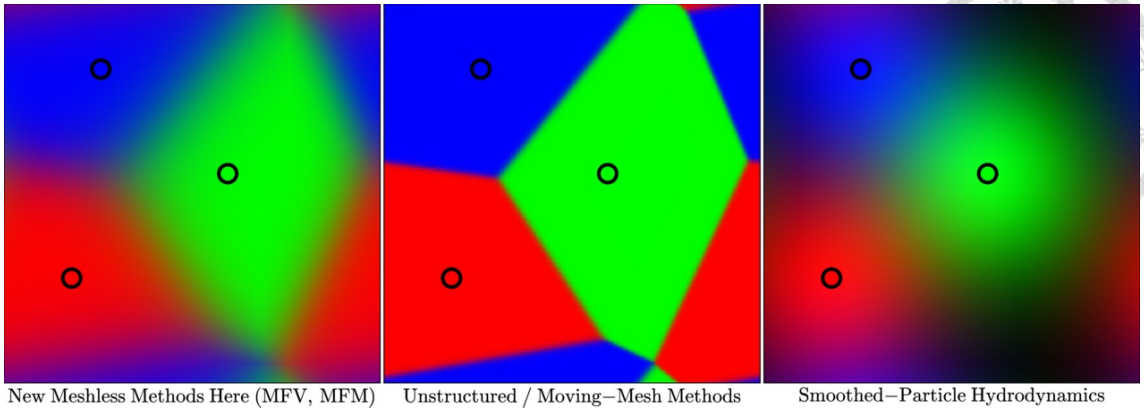

Figure 2.1: Comparisons between MFM/MFV, Mesh, and SPH methods. Left: New methods of MFM/MFV in GIZMO; Center: Mesh Method; Right: SPH method.

As shown in Figure 2.1, the new methods employed in GIZMO exhibit characteristics of Voronoi-based moving-mesh methods but maintain smooth particle transitions near edges, thus preventing discontinuities when the mesh moves. The Voronoi-based moving-mesh methods can be viewed as a special case of the new MFV/MFM methods, where the weighting function W resembles a step function, and the boundaries are determined by the nearest particle.

Finally, the equation describes the Godunov finite-volume equations,

$$\frac{d}{dt}(V_i \mathbf{U}_i) + \sum_j \tilde{\mathbf{F}}_{ij} \cdot \mathbf{A}_{ij} = 0 \tag{2.11}$$

where $\tilde{\mathbf{F}}_{ij} = -\tilde{\mathbf{F}}_{ji}$ and $\mathbf{A}_{ij}^{\alpha} = V_i \tilde{\phi}_j^{\alpha}(\mathbf{x}_i) - V_j \tilde{\phi}_i^{\alpha}(\mathbf{x}_j)$. The first term is the conserved quantities of the particles; $\mathbf{F}_{ij}$ is the flux and ensures the conservation of quantities, and $\mathbf{A}_{ij}^{\alpha}$ is the effective face area.

doi:10.6342/NTU202401221

2.3 Gravity

The gravity in the models includes the self-gravity of gas and dark matter particles. The self-energy of gas particles from gravity can be defined as

$$E_{grav} = \frac{1}{2}\sum_{i,j} G m_i m_j \phi(\mathbf{r}_{i,j}, h_j) \tag{2.12}$$

where $\phi(r_{i,j}, h_j)$ is the potential energy of particles, $\mathbf{r}_{ij} = \mathbf{x}_i - \mathbf{x}_j$. The acceleration of gas particles can hence be described as

$$m_i \frac{d\mathbf{v}_i}{dt}\bigg|_{grav} = -\nabla_i E_{grav} \tag{2.13}$$

The last term is

$$\begin{aligned} -\nabla_i E_{grav} = -\sum_j \Bigg[& \frac{G m_i m_j}{2} \left(\frac{\partial \phi(r, h_i)}{\partial r}\Big|_{r_{ij}} + \frac{\partial \phi(r, h_j)}{\partial r}\Big|_{r_{ji}} \right) \\ & + \frac{G}{2} \left(\zeta_i \frac{\partial W(r, h_i)}{\partial r}\Big|_{r_{ij}} + \zeta_j \frac{\partial W(r, h_j)}{\partial r}\Big|_{r_{ji}} \right) \Bigg] \hat{\mathbf{r}_{ij}} \end{aligned} \tag{2.14}$$

$$\zeta_a = m_a \frac{h_a}{n_a \nu} \frac{1}{\Omega_a} \sum_b m_b \frac{\partial \phi(r_{ab}, h)}{\partial h}\Big|_{h=h_a} \tag{2.15}$$

$$\begin{aligned} \Omega_a &\equiv 1 + \frac{h_a}{n_a \nu} \frac{\partial n_i}{\partial h_i} \\ &= 1 - \frac{h_a}{n_a \nu} \sum_b \left(\frac{r_{ab}}{h_a} \frac{\partial W(r, h_a)}{\partial r}\Big|_{r_{ab}} + \frac{\nu}{h_a} W(r_{ab}, h_a) \right) \end{aligned} \tag{2.16}$$

doi:10.6342/NTU202401221

The first line in 2.14 represents the $\nabla\Phi$ where h is fixed. The second line represents the part where h is changed when the particles move.

The calculation for the non-gaseous particles, for example, dark matter particles, is similar to the gas particles.

2.4 Gas Properties

In this study, our goal is to understand the gas properties around the star-forming clouds in the early universe. To achieve this, we need to make several assumptions about the initial conditions of the primordial gas cloud. These assumptions are crucial for setting up the simulation accurately and ensuring that the results are meaningful. The parameters we used are listed in Table 2.2.

Parameters	Description	Values	Unit
m_p	Mass of Proton	1.67×10^{-24}	[g]
X_H	Gas Fraction	0.76	-
x_e	Electron Abundance	Values In File	[g]
μ	Mean Molecular Weight	Derived Values	[g]
E_u	Internal Energy	Values In File	[erg]
k_B	Boltzmann Constant	1.38×10^{-16}	[erg/K]
γ	Adiabatic Index	5/3	-

Table 2.2: Parameters of Gas Properties

In general, we assume the gas particles to be ideal gas where $\gamma = 5/3$. The composition of the primordial cloud is 76% H and 24% He. The temperature of the gas can be calculated by the following formula

$$\mu = \frac{4}{1 + 3X_H + 4X_H x_e} * m_p \tag{2.17}$$

doi:10.6342/NTU202401221

$$T = (\gamma - 1) * \frac{E_u}{k_B} * \left(\frac{\textit{Unit Energy}}{\textit{Unit Mass}} \right) * \mu \tag{2.18}$$

where γ is the adiabatic index, E_u is the internal energy per unit mass of gas particles, k_B is the Boltzmann constant, and μ is the mean molecular mass of gas particles.

2.4.1 Cooling

Since the environment of primordial star-forming clouds at $z \approx 20$ is metal-free and dust-free due to the absence of star-formation history, the primordial cloud is dominated by hydrogen and helium. The virial temperature, which is related to the virial velocity of DM, can be approximated by $k_B T_{vir} \sim m_H v_{vir}^2$ (Bromm, 2013):

$$T_{vir} \cong 2 \times 10^3 \text{ K} \left(\frac{M_h}{10^6 M_\odot} \right)^{2/3} \left(\frac{1+z}{20} \right) \tag{2.19}$$

suggests that the gas particles in the mini-halos have a temperature around 10^4 K.

In our model, we consider the primordial radiative heating and cooling given by GIZMO and GRACKLE (Hopkins et al., 2018; Smith et al., 2017). GRACKLE, which is the external chemical library that could better solve the environment of primordial clouds (Smith et al., 2017), contains the primordial chemistry network for atomic H, D, He, and molecules HD, H_2. The cooling and heating rate per unit volume can be described as the sum of all processes:

$$\frac{de^a_{thermal}}{dt} = -n^2_{H,a} \Lambda^a_{net} = -n^2_{H,a} \sum_i \Lambda_i \tag{2.20}$$

where $de^a_{thermal}$ is the density of thermal energy of gas species a, and Λ represents both

doi:10.6342/NTU202401221

the cooling and heating rates, only differs in the sign (the positive sign denotes cooling processes, and vice versa).

The cooling has the following processes (Hopkins et al., 2018; Katz et al., 1996):

1. Collisional excitation: H^0, He^+.

2. Collisional ionization: H^0, He^0, He^+.

3. Recombination: H^+, He^+, He^{2+}.

4. Free-free emission: All ions.

For photon-ionization and photon-heating computed with the photo-ionization code CLOUDY (Ferland et al., 2017), we make assumptions about the UV background in our simulation from Faucher-Giguère et al. (2009) and Haardt & Madau (2012). However, since our model prevents the birth of newborn stars, UV background is not a dominant effect. On the other hand, gas temperature in the mini-halo usually doesn't exceed the threshold $\sim 10^4$ K, where the atomic cooling is less efficient. Hence, H_2 is the major coolant in our model.

H_2 cooling becomes dominated where enough hydrogen molecules are produced in the dense area ($\geq 10^4$ cm^{-3}). Producing hydrogen molecules by colliding two hydrogen atoms is difficult because of the symmetry of molecules. The consequences of the symmetry lead to the difficulty of radiating the energy through rapid electric dipole, and finally cause the binding system to decay. The more important processes are from two channels

doi:10.6342/NTU202401221

(Bromm, 2013; Saslaw & Zipoy, 1967):

$$
\begin{aligned}
H + e^- &\longrightarrow H^- + \gamma \\
H^- + H &\longrightarrow H_2 + e^-
\end{aligned}
\tag{2.21}
$$

and,

$$
\begin{aligned}
e^- + H^+ &\longrightarrow H \\
H + H^+ &\longrightarrow H_2^+ + \gamma \\
H_2^+ + H &\longrightarrow H_2 + H^+ \\
H_2 + H &\longrightarrow 3H
\end{aligned}
\tag{2.22}
$$

where γ is a photon. The second and the third equations in Eq (2.22) can form a cycle, and the photon from the second line can further produce many hydrogen molecules. The last line indicates the dissociation of hydrogen molecules, but this is negligible for the environment below 6000 K.

The low-temperature cooling methods are mainly developed by (Hopkins et al., 2018; Hopkins et al., 2022), which can let the cooling processes extend to $\sim$ 10 K. In our model, we solve the hydrogen molecular fraction with GRACKLE cooling network.

2.5 Initial Conditions

To run high-resolution zoom-in simulations, we cannot directly feed the entire snapshot of TNG50-1 into GIZMO due to the excessive number of particles. Instead, the IllustrisTNG project provides sub-halo search tools based on SUBFIND algorithm that allow us to capture information on gas and dark matter from individual halos. Typical mini-halos

doi:10.6342/NTU202401221

have a mass around 10^7 $M_\odot$, which is also close to the detection limit for sub-halos. Our goal is to identify suitable mini-halos in TNG50-1 and use them as initial conditions for our zoom-in simulations. The criteria for selection are as follows:

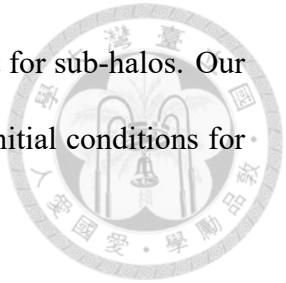

1. Find the mini sub-halos (total mass $\leq 10^7$ $M_\odot$) that could be identified in TNG50-1 at $z \approx 20$.

2. The identified sub-halos must be the dominant sub-halo in the parent halo.

3. Check out whether there is a merger event that happened between the current snapshot (index=0, $z \approx 20$) and the next snapshots (index=1, $z \approx 15$). If true, consider both sub-halos; if not, consider an isolated case. Here, we mainly focus on the isolated cases.

Finally, we chose the first 31 results in our query as the initial conditions and validated 26 of them for the final simulations. The total masses of them range from 7.25×10^6 $M_\odot$ to 2.45×10^7 $M_\odot$. The details of the initial conditions are listed in Table 2.3.

Since every initial condition only includes no more than 100 particles (the resolutions in TNG are 8.5×10^4 $M_\odot/h$ for gas and 4.5×10^5 $M_\odot/h$ for DM, respectively, listed in Table 2.1). To achieve the desired level of detail and accuracy, it is necessary to split each particle into smaller ones before or during the simulations. The next section will describe the particle splitting algorithm in detail, explaining how it is implemented and how it contributes to the enhancement of our simulation's resolution.

doi:10.6342/NTU202401221

Subhalo ID	Gas Mass $\log_{10}$ [$M_\odot$/h]	Dark Matter Mass $\log_{10}$ [$M_\odot$/h]	Particle Range [ckpc/h]	Matter Density $\log_{10}$ [g/cm^3]
31590	6.02	6.86	12.73	-23.65
31812	5.96	6.86	16.71	-24.01
30331	6.01	6.86	17.86	-24.10
30779	5.99	6.89	13.70	-23.73
31393	5.98	6.89	14.28	-23.78
29124	6.00	6.89	16.51	-23.97
31859	5.93	6.89	12.90	-23.66
29773	5.97	6.91	16.97	-23.99
31708	5.89	6.91	17.19	-24.01
31869	5.91	6.91	13.48	-23.69
28336	6.01	6.91	15.47	-23.86
27836	6.03	6.91	19.89	-24.19
30476	6.00	6.91	14.49	-23.78
30112	5.98	6.91	16.31	-23.94
28585	5.98	6.91	14.90	-23.82
27261	6.00	6.93	15.94	-23.88
28323	5.96	6.93	16.36	-23.92
26842	5.98	6.93	15.05	-23.81
28199	5.99	6.93	14.85	-23.79
27062	6.01	6.93	17.29	-23.99
27856	5.98	6.96	24.91	-24.45
27075	5.96	6.96	13.33	-23.63
28904	5.97	6.96	16.93	-23.94
30251	6.34	7.27	25.54	-24.16
26616	6.35	7.28	25.39	-24.14
26221	6.42	7.38	30.36	-24.28

Table 2.3: Parameters of Initial Conditions

2.6 Cosmology Zoom-in Simulation

In order to thoroughly examine the gas properties in dense regions of the early universe, it is essential to split both gas and dark matter particles from the original simulation. The initial mass resolutions of TNG50 are 8.5×10^4 $M_\odot$ for gas particles, and 4.5×10^5 $M_\odot$ for dark matter particles.

Our goal for the zoom-in simulation is to investigate the gas properties of mini-halos, which typically have a size of around 100 pc. To effectively analyze the turbulence pro-

doi:10.6342/NTU202401221

duced in the simulation, we aim to achieve a mass resolution of approximately $0.1\ M_\odot$ for gas particles and $200\ M_\odot$ for dark matter particles.

The splitting algorithm is as follows:

Criterion Check for Splitting: Determine if a particle meets the criteria for splitting. Specifically, a gas particle is eligible for splitting if its mass exceeds $2 \times 0.1\ M_\odot$ and a dark matter particle is eligible if its mass exceeds $2 \times 200\ M_\odot$.

Determining Particle Spacing: Before splitting a particle, determine the spacing of the new particles. The code searches for the nearest particle to the target particle and then calculates the effective radius based on the distance between them or the softening length. The spacing distance is set to 0.7 times the effective radius or 0.5 times the softening length if using a cubic spline kernel.

Splitting the Particle: For each target particle, a new particle is created, each carrying half the mass of the original particle. The positions of the two resulting particles are adjusted randomly within a specified direction and separated by the previously determined distance while maintaining the center of mass of the original particle.

Triggering the Splitting Check: The splitting check is triggered every time the domain is decomposed in the simulation.

In summary, the algorithm effectively splits a particle into two particles, each with half the mass of the original particle, ensuring the conservation of mass, energy, and momentum. This method minimizes the introduction of ”noise” during the splitting process, allowing for a more accurate and stable simulation.

By employing this particle splitting algorithm, we can achieve the desired mass res-

doi:10.6342/NTU202401221

olution, thereby enabling a more detailed and precise analysis of gas properties and turbulence in mini-halos.

doi:10.6342/NTU202401221

Chapter 3 Results

In this chapter, we present the results of our simulations. Due to computational resource limitations, we selected snapshot_030 for analysis across all models to facilitate better comparison. Consequently, the simulations span from $z \approx 20$ to $z \approx 19.40$, which corresponds to approximately 7.95 million years in cosmic time. The subsequent sections include rendering plots of density and temperature, compression, vorticity, the Kolmogorov spectrum, phase diagrams, and the turbulence Mach number derived from our simulations.

To demonstrate the stability of the particle splitting method employed in our simulations, we conducted convergence tests, with the results presented in Appendix A.1 to A.3.

3.1 Rendering Plots of the Density and Temperature

In this section, we present the rendering plots of density and temperature for four models: sub-halo 31590, sub-halo 28336, sub-halo 26616, and sub-halo 27856. These models were chosen to represent a range of average matter densities, from high to low. The results are displayed in Figures 3.1, 3.2, 3.3, and 3.4.

doi:10.6342/NTU202401221

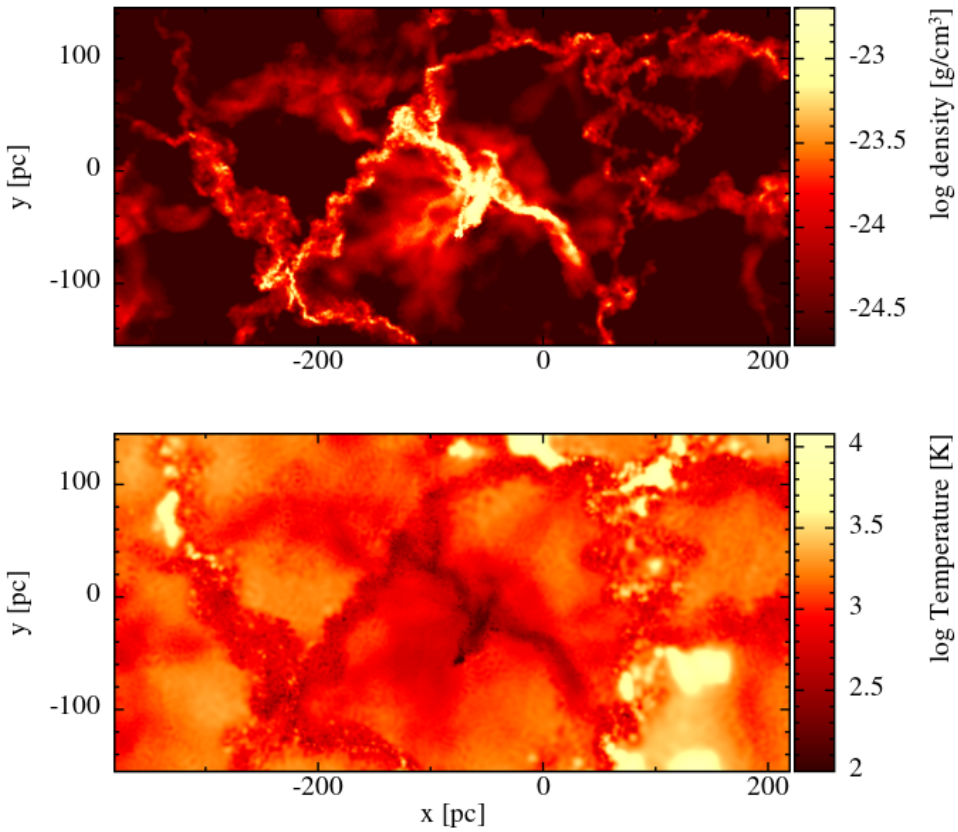

Figure 3.1: Rendering plot of the density and temperature of sub-halo 31590. Top panel: Slice plot of the density. Bottom panel: Slice plot of the temperature.

doi:10.6342/NTU202401221

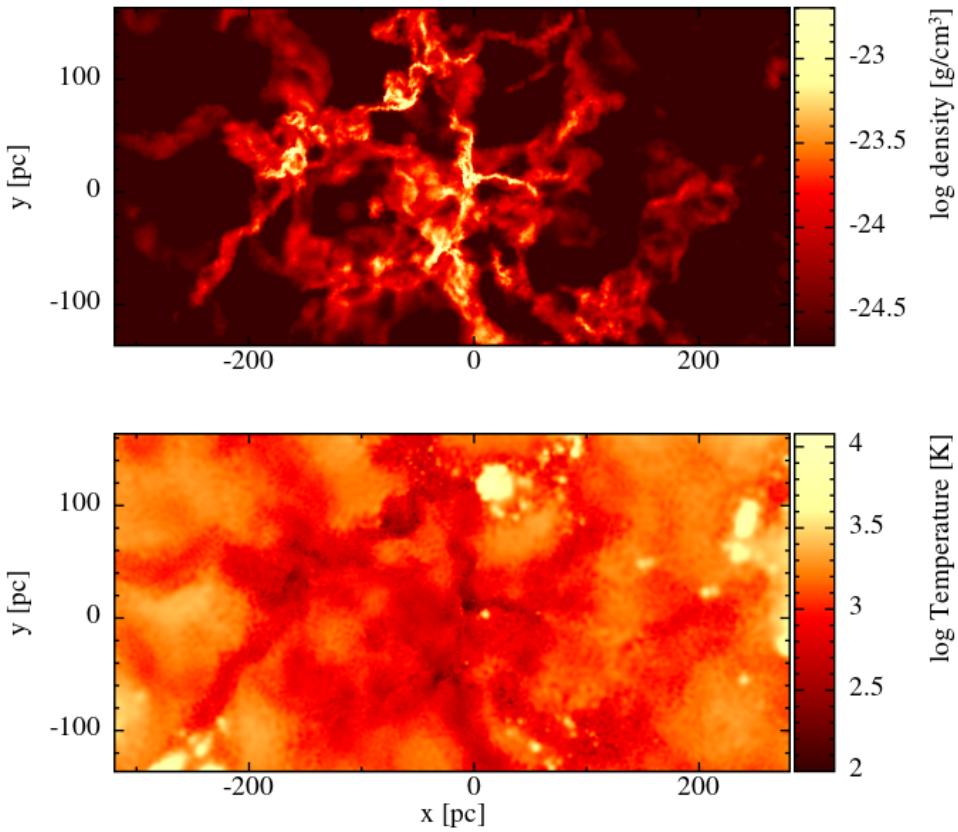

Figure 3.2: Rendering plot of the density and temperature of sub-halo 28336. Top panel: Slice plot of the density. Bottom panel: Slice plot of the temperature.

doi:10.6342/NTU202401221

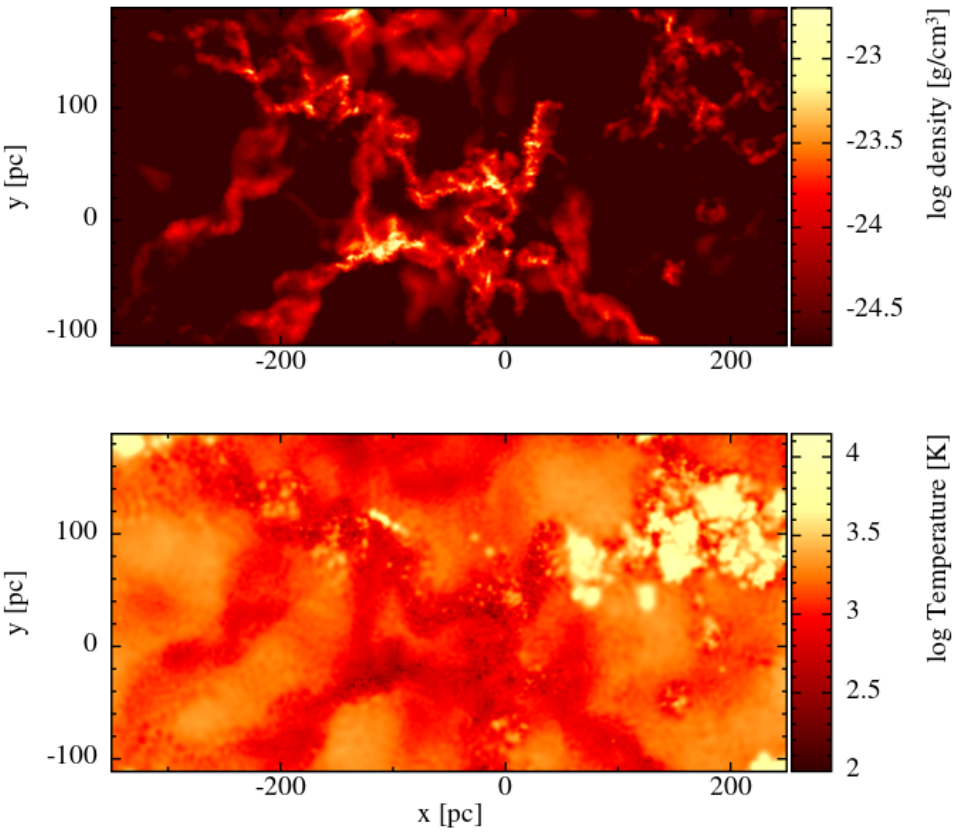

Figure 3.3: Rendering plot of the density and temperature of sub-halo 26616. Top panel: Slice plot of the density. Bottom panel: Slice plot of the temperature.

doi:10.6342/NTU202401221

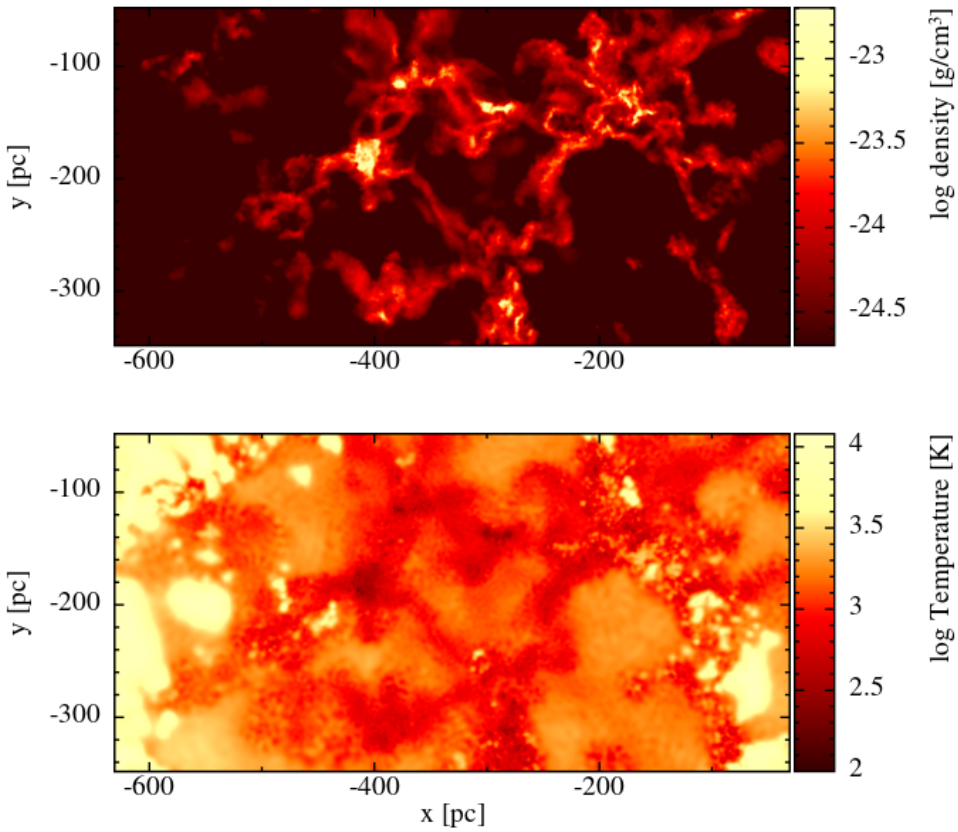

Figure 3.4: Rendering plot of the density and temperature of sub-halo 27856. Top panel: Slice plot of the density. Bottom panel: Slice plot of the temperature.

doi:10.6342/NTU202401221

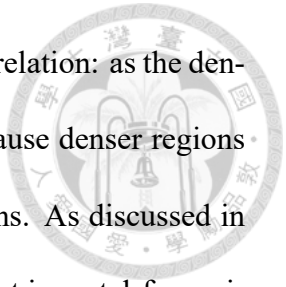

The rendering plots of density and temperature reveal an inverse relation: as the density increases, the temperature decreases. This trend is expected because denser regions tend to produce more molecular hydrogen compared to diffuse regions. As discussed in the previous chapter, molecular hydrogen serves as the primary coolant in metal-free primordial clouds.

Consequently, dense regions exhibit more efficient cooling due to the higher concentration of molecular hydrogen. This relation will be further substantiated in Section 3.4, where we analyze the phase diagrams to corroborate the cooling behavior in different density regions.

To demonstrate the evolution of density and temperature in our simulation, we present time-series density and temperature plots for sub-halo 27075. This model is also used to perform convergence tests, and the snapshots are taken at redshifts $z \approx 19.71$, 19.28, and 18.86. The projection plots of density and temperature are displayed in Figures 3.5, 3.6, and 3.7.

The comparison between the distribution of gas density and temperature in sub-halo 27075 shows consistent trends with our previous discussions. The time-series plots provide a detailed view of the gas collapse processes within the halo. Figure 3.5 is the first snapshot after the particles have been split. The errors introduced by splitting can disrupt the initial conditions and affect subsequent evolution. However, the error could be eliminated by the simulation code when the simulation continues.

Therefore, minimizing the time between the start of the simulation and the completion of particle splitting is crucial. Early splitting ensures that the simulation has ample time to correct any introduced errors, resulting in more reliable and stable results in the later

doi:10.6342/NTU202401221

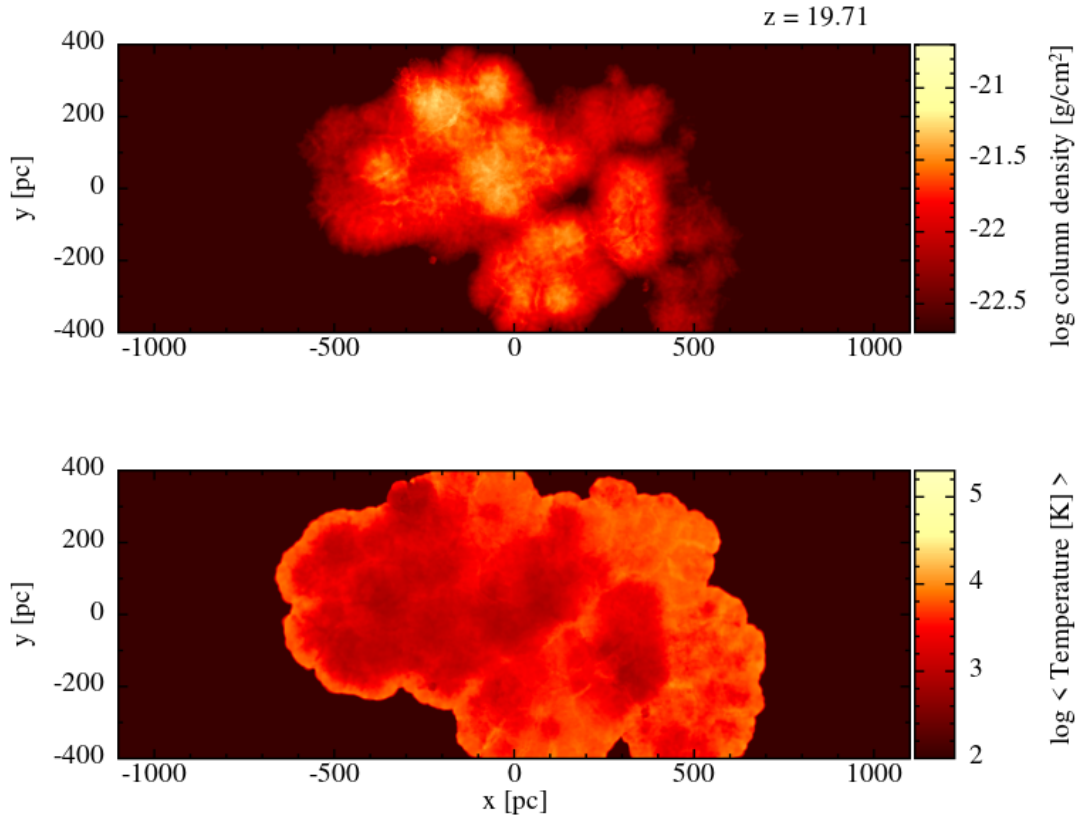

Figure 3.5: Rendering plot of the density and temperature of sub-halo 27075 at z ≈ 19.71. Top panel: Projection plot of the density. Bottom panel: Projection plot of the temperature.

doi:10.6342/NTU202401221

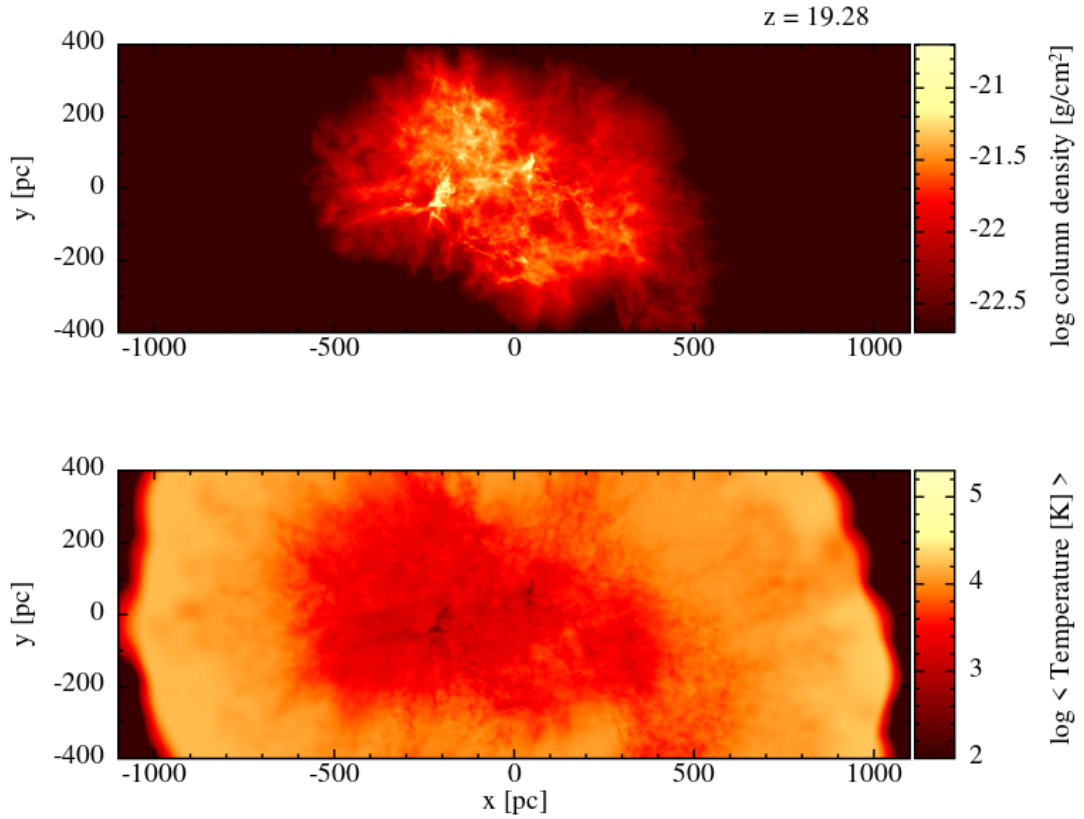

Figure 3.6: Rendering plot of the density and temperature of sub-halo 27075 at z ≈ 19.28. Top panel: Projection plot of the density. Bottom panel: Projection plot of the temperature.

doi:10.6342/NTU202401221

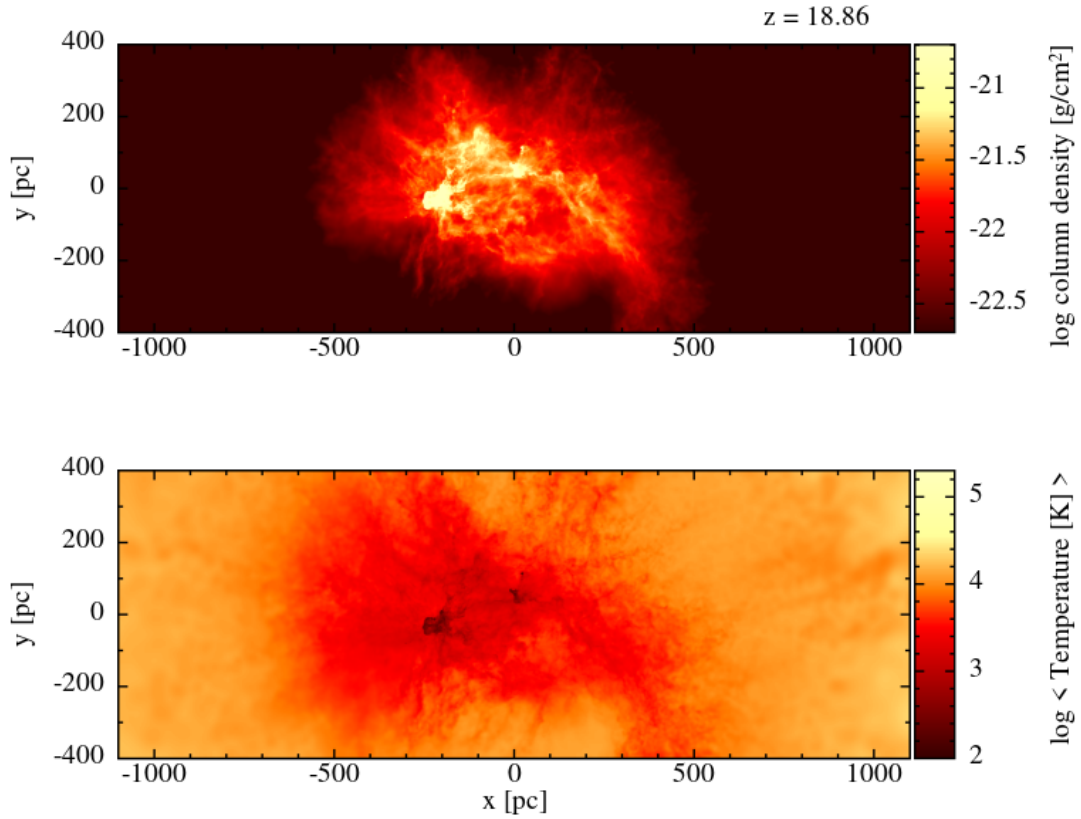

Figure 3.7: Rendering plot of the density and temperature of sub-halo 27075 at z ≈ 18.86. Top panel: Projection plot of the density. Bottom panel: Projection plot of the temperature.

doi:10.6342/NTU202401221

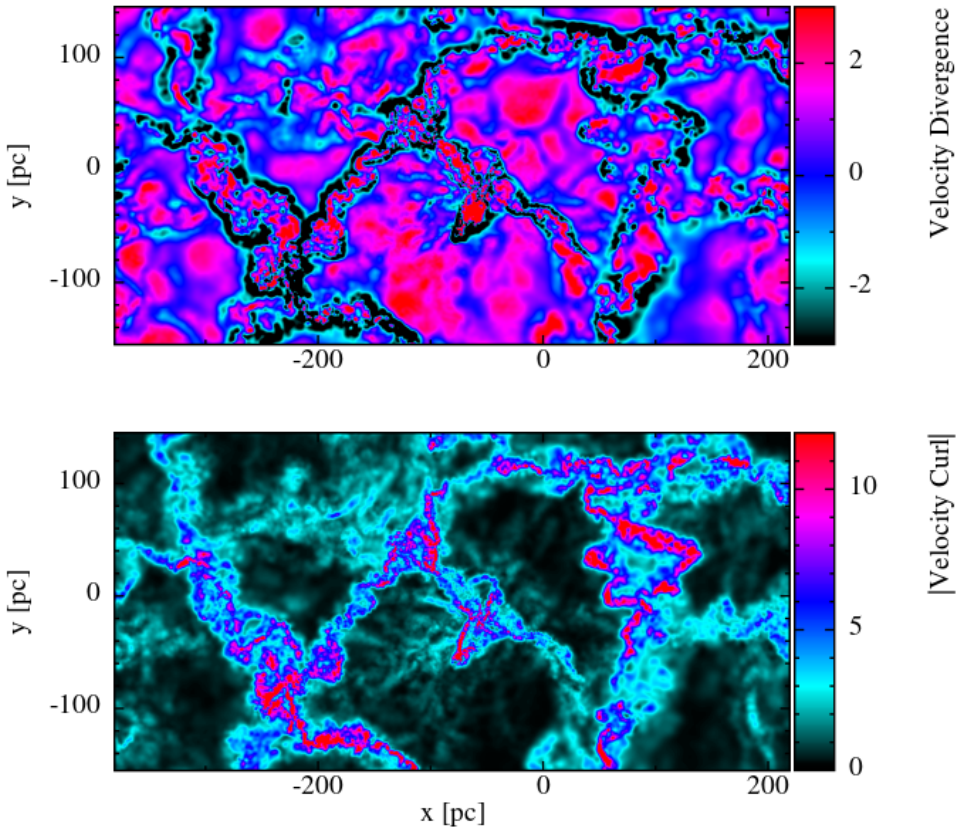

Figure 3.8: Gas compressibility and vorticity of sub-halo 31590. Top panel: Velocity divergence. Bottom panel: Velocity vorticity.

stages.

3.2 Gas Compression and Vorticity

The compression of the gas can be derived from the divergence of the velocity field, while the vorticity is obtained from the curl of the velocity field. The results for sub-halos 31590, 28336, 26616, and 27856 are shown in Figures 3.8, 3.9, 3.10, and 3.11.

When examining these plots alongside the density and temperature results from the previous section, it becomes evident that the divergence and curl of the velocity field exhibit significant variations in the centers of dense regions. This indicates that gas in these areas is subject to high compression and vorticity, making these regions critical for

doi:10.6342/NTU202401221

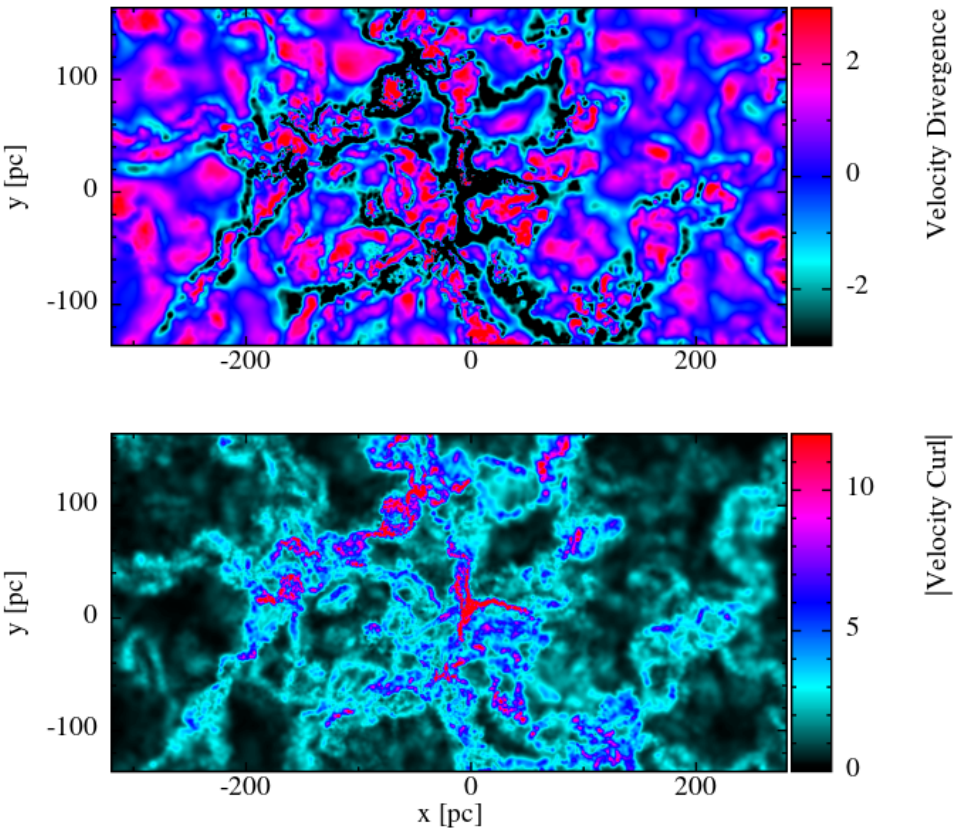

Figure 3.9: Gas compressibility and vorticity of sub-halo 28336. Top panel: Velocity divergence. Bottom panel: Velocity vorticity.

doi:10.6342/NTU202401221

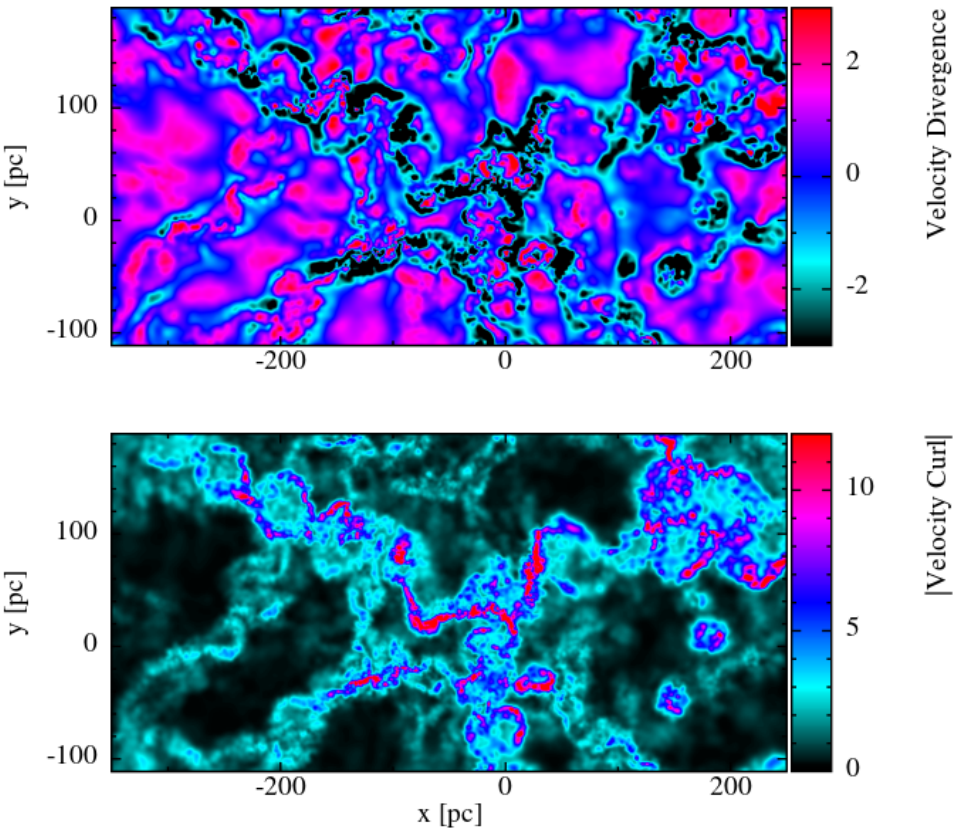

Figure 3.10: Gas compressibility and vorticity of sub-halo 26616. Top panel: Velocity divergence. Bottom panel: Velocity vorticity.

doi:10.6342/NTU202401221

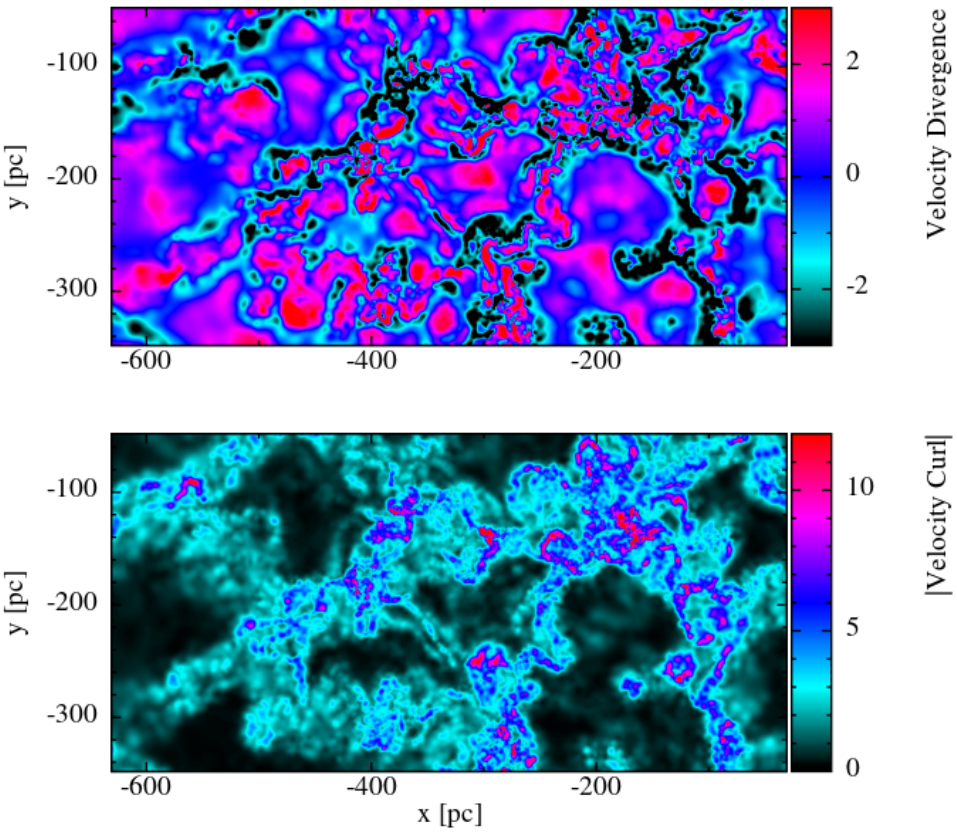

Figure 3.11: Gas compressibility and vorticity of sub-halo 27856. Top panel: Velocity divergence. Bottom panel: Velocity vorticity.

doi:10.6342/NTU202401221

analyzing the strength of turbulence.

These findings underscore the importance of focusing on the central dense areas within the sub-halos, as these regions exhibit the most intense dynamical activity. The high compression and vorticity within these areas are key indicators of the turbulent processes that play a crucial role in the evolution and behavior of the primordial gas clouds.

3.3 Kolmogorov Spectrum

To understand the relation between energy and the scale of turbulence, we calculated the Kolmogorov spectrum. Using YT to load data and PYTHON to calculate the energy spectrum across different scales (wave numbers), we derived several normalized curves of the energy power spectrum. These curves were then combined according to their k values to provide a comprehensive view of the energy distribution across scales.

The Kolmogorov spectrum consists of three phases: energy-containing, inertial, and dissipation. The energy-containing phase indicates where the energy of turbulence is increasing due to energy sources. In the inertial phase, turbulence remains constant. Finally, in the dissipation phase, the energy of turbulence begins to decay.

Given that turbulence can persist down to scales of $\sim$ m, it is impractical for us to observe the dissipation phase within our simulations. However, the energy-containing phase is observable. A characteristic of this phase is a flat slope in the low-k region, signifying that the energy of turbulence has not yet fully developed and is still accumulating.

The endpoint of the energy-containing phase, which also marks the beginning of the inertial phase, indicates the scale that has a significant impact in the center of the mini-

doi:10.6342/NTU202401221

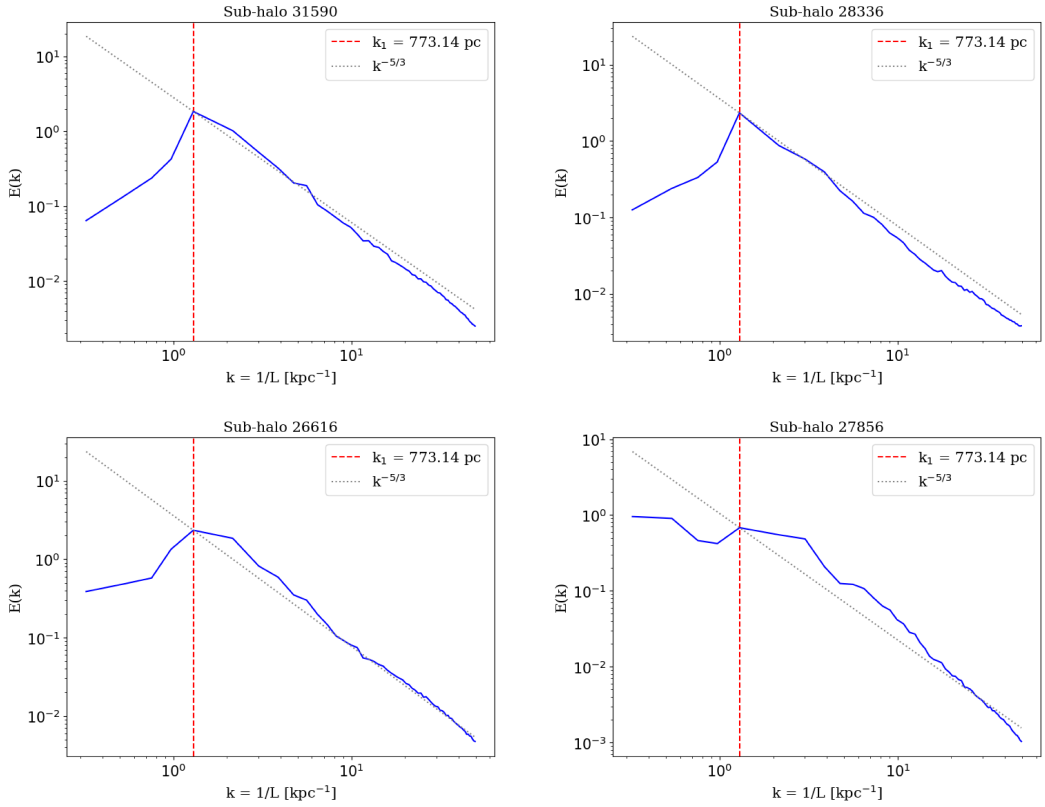

Figure 3.12: Kolmogorov Spectrum. We show the Kolmogorov spectrum for four sub-halos. The x-axis represents the turbulence wave numbers with the unit [kpc^{-1}]; the y-axis represents the normalized turbulence energy.

doi:10.6342/NTU202401221

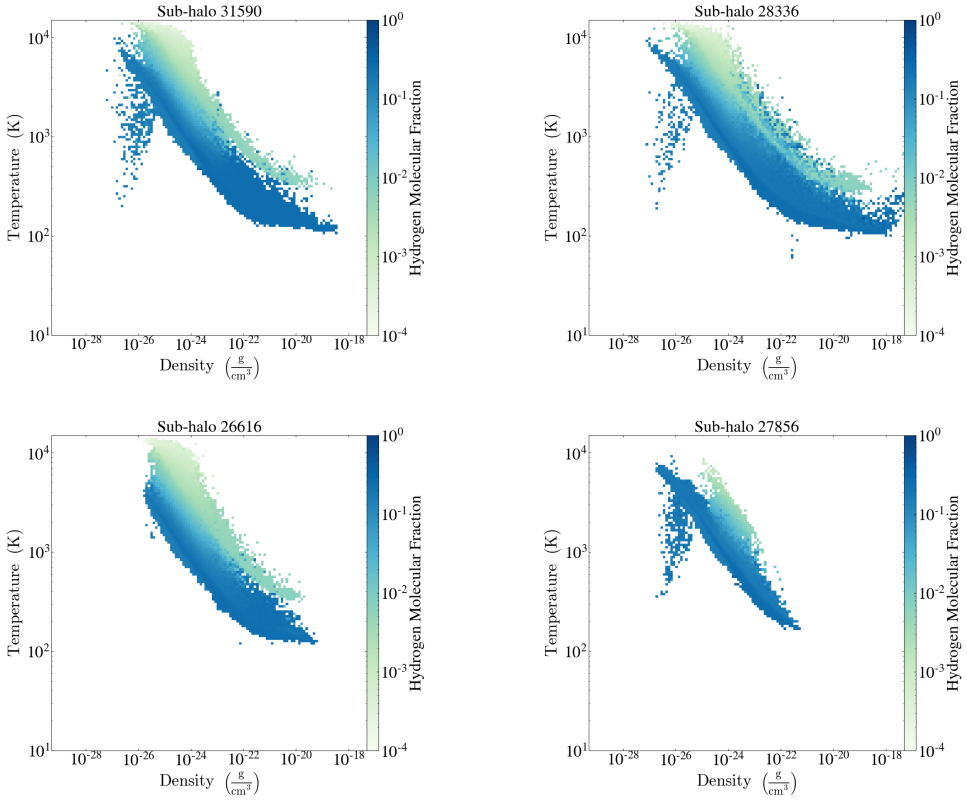

Figure 3.13: Phase diagram of the sub-halos. The x-axis is the gas density; the y-axis is the gas temperature; the color bar shows the H_2 Fraction. The darker grid shows the higher fraction of the H_2 Fraction.

halo. The physical scale is derived from $k = 1/l_0$. In Figure 3.12, we observe that the turning point of the energy-containing phase is around $k \sim 10^0$ in units of kpc^{-1}. Thus, the physical scale for this k value is approximately 1 kpc.

Considering the mini-halo's $R_{200} \approx 250 \sim 350$ pc, the physical scale of the largest turbulence is about two times the scale of the mini-halo. This insight provides clues about how wide the outskirts area should be considered when simulating mini-halos.

3.4 Phase Diagram

The phase diagram of the dense area of the sub-halo 31590, 28336, 26616, and 27856 are shown in Figure 3.13.

doi:10.6342/NTU202401221

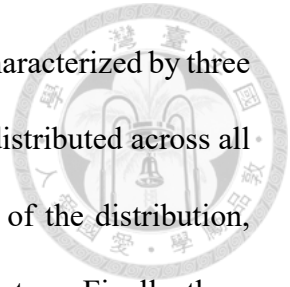

Our results display similar distributions across all four models, characterized by three main features: First, it shows that large amounts of gas particles are distributed across all temperatures but with low density. Second, there is a narrow band of the distribution, which is extended from low density to high density with a low temperature. Finally, there are some scatter distributions in the very high-density area with different temperatures.

Wide Temperature Distribution in Low-Density Regions: The first feature is a large number of gas particles distributed across a wide range of temperatures but maintaining low densities. This can be attributed to the cooling process in our models. Initially, the simulations start with diffuse, high-temperature gas. As the simulations progress, the gas cools down gradually while falling toward the center of the halo.

Narrow Band from Low to High Density with Low Temperature: The second feature is a narrow band extending from low to high densities while maintaining a low temperature. This indicates that the gas remains at a low temperature as its density increases. From the previous section, we observed that higher vorticity values and negative divergence are coupled with the dense areas in the center of the mini-halo. This band describes the process of gas undergoing strong compression and vorticity.

Scattered Distributions in Very High-Density Regions: The third feature is the presence of scattered points in very high-density areas, exhibiting varying temperatures. This feature indicates the formation of gas clumps within the simulations. These clumps could represent potential star-forming regions. However, it is also possible that these clumps result from instabilities early in the simulation, leading to premature clump formation.

doi:10.6342/NTU202401221

3.5 Characteristic Turbulence Mach Number

In this section, we calculate the characteristic turbulence Mach number in our simulation. The turbulence Mach number is related to the velocity dispersion and the sound speed in the local velocity field. The speed of sound of the gas can be calculated by:

$$c_s = \sqrt{\frac{\gamma \cdot R \cdot T}{\mu \cdot m_p}} \tag{3.1}$$

where T is the temperature, γ is the adiabatic index for the gas, R is the gas constant, m_p is the mass of a proton, and μ is the mean molecular weight given by Eq. 2.17. The Mach number of the gas can be further calculated by

$$\mathcal{M} = v/c_s \tag{3.2}$$

where v represents the velocity dispersion of gas. We selected gas densities exceeding 10^5 times the critical density as a reference and calculated the velocity dispersion for the neighboring 32 gas particles. Using these values, we calculated the sound speed of the target particles and obtained the Mach number using Eq. 3.2.

The results are shown in the figure 3.14. We produced two plots for the Mach number relations: one showing the Mach number relative to the total mass of the halo, and the other showing the Mach number relative to the average matter density of the halo. Also, we calculate the Mach number within the virial radius defined by ρ_{200}. We calculate the magnitude of velocity for every gas particle instead of the method of the local velocity dispersion we mentioned in the previous passage.

Figure 3.14 does not show a clear correlation between the strength of the turbulence

doi:10.6342/NTU202401221

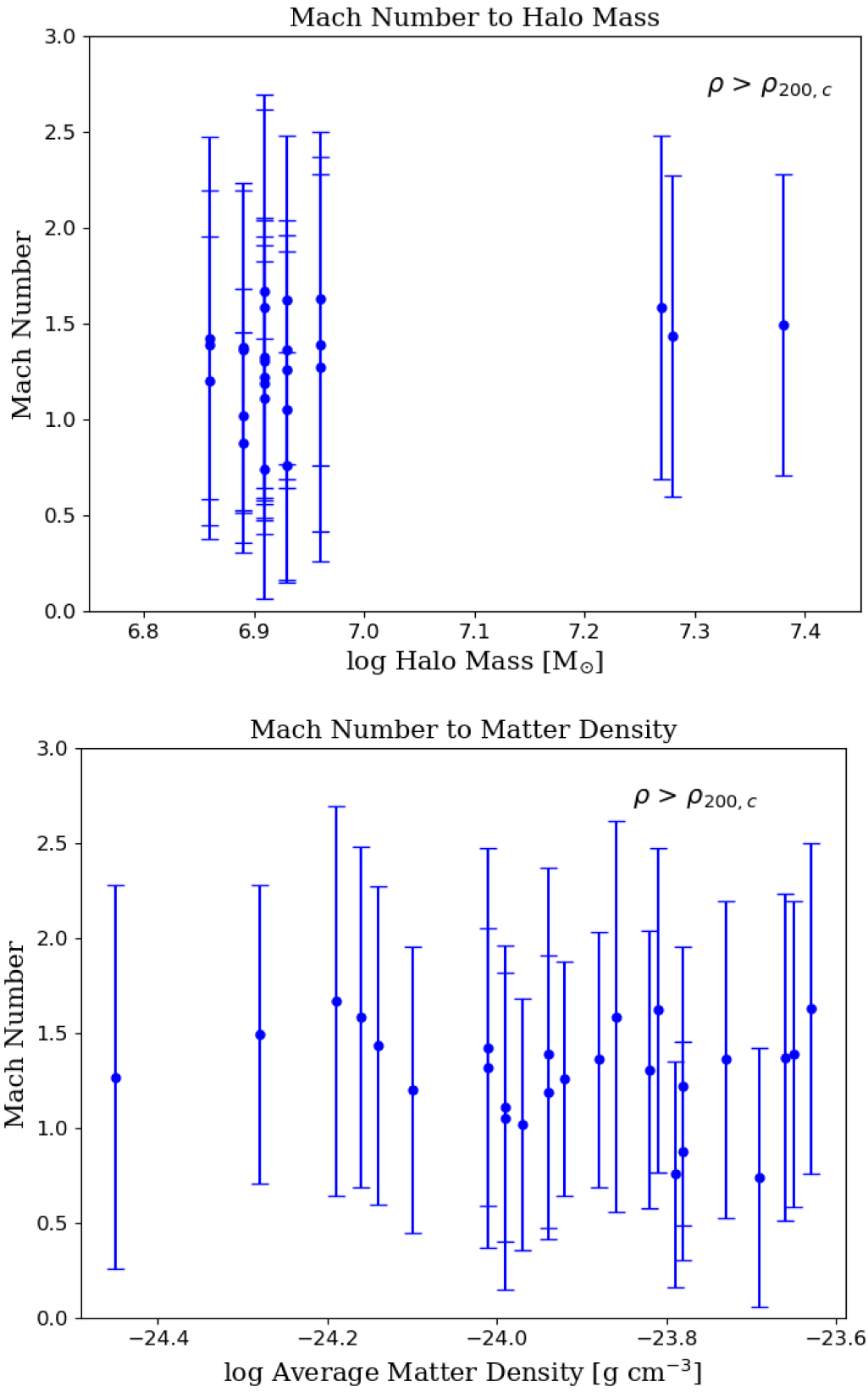

Figure 3.14: Mach Number to Initial Conditions. Top panel: Mach number to the initial halo mass. Bottom panel: Mach number to the initial matter density. The x-axis is the initial halo mass and average matter density; the y-axis is the Mach number calculated by the local velocity dispersion of every gas particle divided by the sound speed.

doi:10.6342/NTU202401221

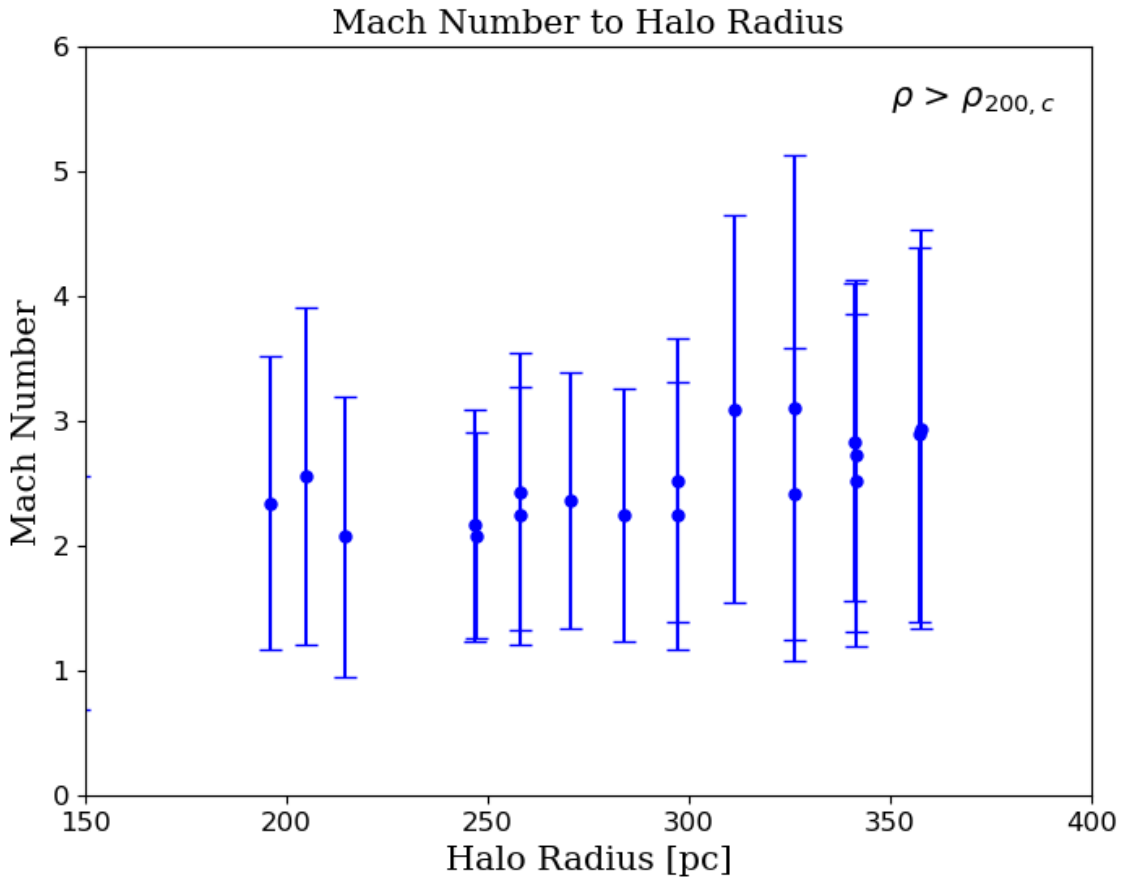

Figure 3.15: Mach number to the Halo Radius. The x-axis is the halo radius defined by ρ_{200}; the y-axis is the Mach number calculated by the magnitude of the gas velocity divided by the sound speed.

doi:10.6342/NTU202401221

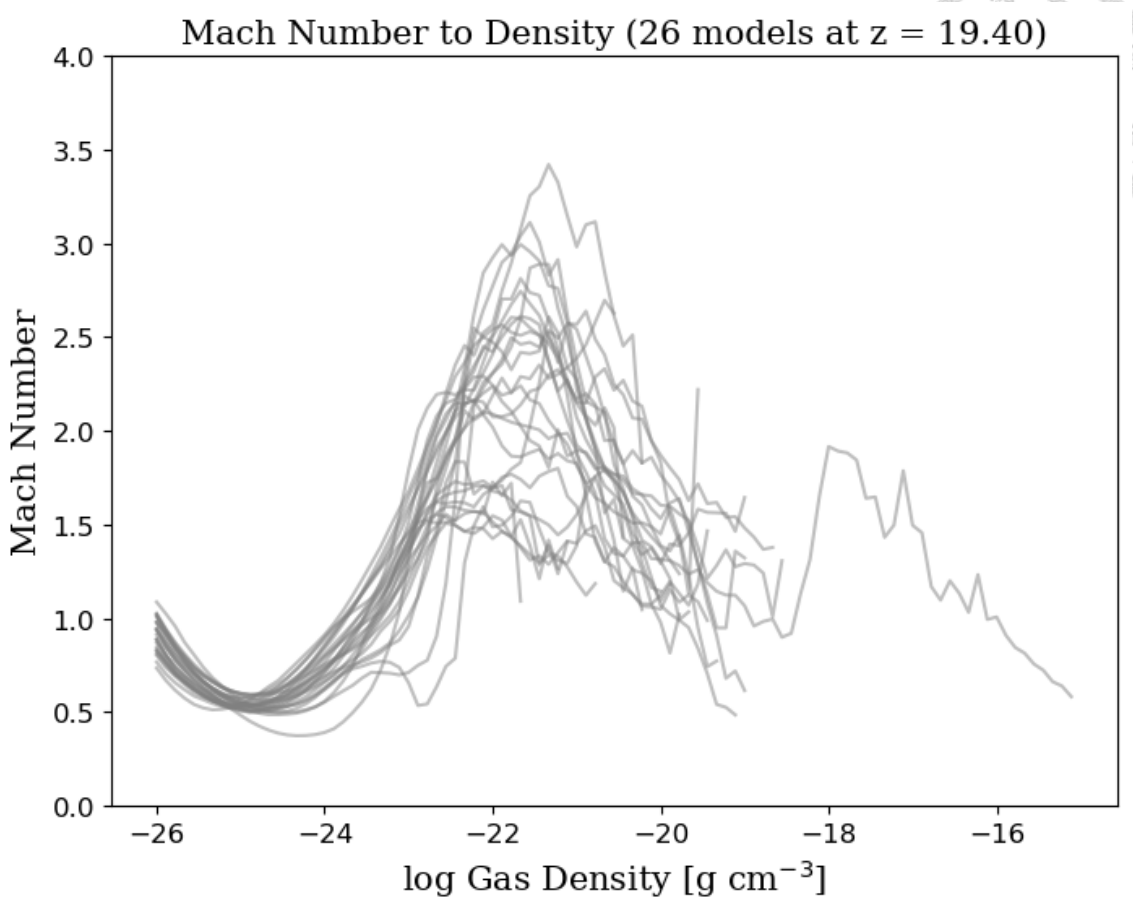

Figure 3.16: Curves version: Mach number to the local density. The x-axis is the local gas density; the y-axis is the Mach number calculated by the velocity dispersion method.

and the initial conditions of our models. Figure 3.15 shows the slightly stronger turbulence when the virial radius is increasing, but the error bar is wide in for every model. However, we found that the strength of the turbulence is more sensitive to the local density. We performed the same process of calculating the Mach number but divided the results into several density bins ranging from $10^{-23} \sim 10^{-13}$ g cm^{-3}. The results of the Mach number relative to the local density are presented in Figures 3.16 and 3.17.

The figures 3.17 show the relation between the turbulence Mach number and the local density. We found that the Mach number starts at $\mathcal{M} = 0.91 \pm 0.75$ and increases as the local density rises from 10^{-26} to 2.78×10^{-22} g cm^{-3}. The Mach number reaches a maximum of $\mathcal{M} = 2.20 \pm 1.67$ at $\sim 2.78 \times 10^{-22}$ g cm^{-3}. The Mach number drops after

doi:10.6342/NTU202401221

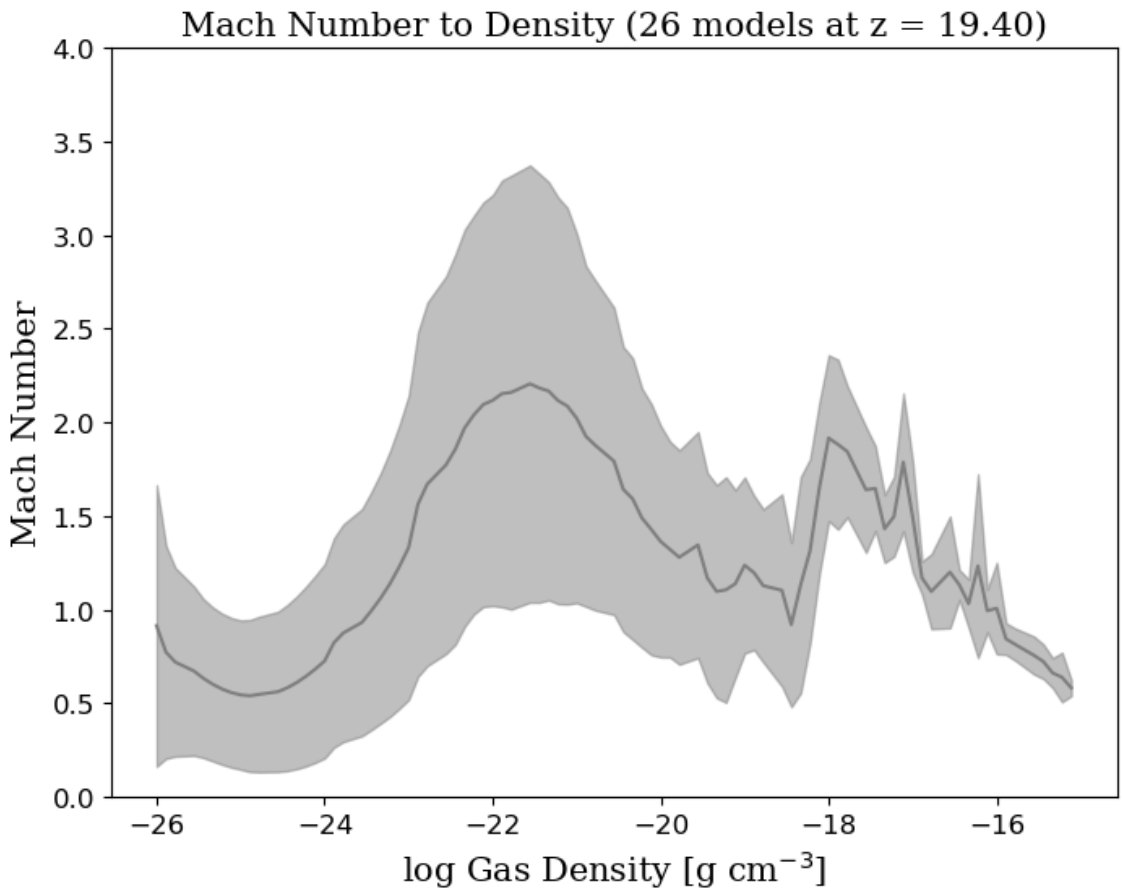

Figure 3.17: Error band version: Mach number to the local density. The x-axis is the local gas density; the y-axis is the Mach number calculated by the velocity dispersion method.

doi:10.6342/NTU202401221

$\sim 10^{-22}$ g cm^{-3} and reaches a minimum value around $\sim 10^{-16}$ g cm^{-3} with the Mach number $\mathcal{M} = 0.58 \pm 0.04$, which is close to the level at the low-density region.

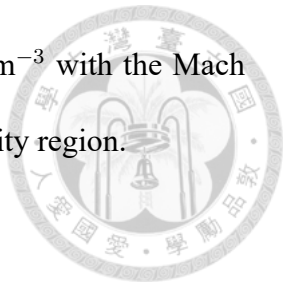

doi:10.6342/NTU202401221

doi:10.6342/NTU202401221

Chapter 4 Discussion

4.1 Zoom-In Noise

The noise produced when proceeding particle splitting method is a serious issue in zoom-in simulations.

New particles may result in local potential wells. Fortunately, by examining the time-series plots of the model in GIZMO, this issue can be mitigated if we perform an appropriate splitting algorithm and complete it at an early stage. Initially, noise can be observed after the particles have been split. However, after a short period, the noise averages out with the surrounding particles.

As a result, zoom-in noise is produced in the simulation every time we perform a particle split, but it can be eliminated by the code once the algorithm adheres to the conservation of mass, energy, and momentum. Nevertheless, the results are easily affected by the initial conditions. If particle splitting is performed after the simulation has run for a while, some over-density areas may form too early, causing the code to slow down after only a few million years.

doi:10.6342/NTU202401221

4.2 Resolution of Gas and Dark Matter

Another important issue is the resolution of particles in our simulation. Increasing the resolution allows us to track the smallest structures within mini-halos, which is crucial for studying turbulence.

However, higher resolution comes with the cost of increased computation time. Even though the code has been optimized by adapting the TreePM algorithm to build the particle structure and compute gravitational forces, it still runs with O(n log n) time complexity. This means that if we increase the resolution by a factor of ten, the computation time increases by at least a factor of approximately 23. If particles cluster too quickly, the TreePM algorithm becomes less accurate, forcing the code to revert to the traditional analytical method with $O(n^2)$ time complexity. In this case, increasing the resolution by tenfold results in a hundredfold increase in computation time.

In our simulation, mini-halos with masses around 10^7 $M_\odot$ typically contain more than 5×10^6 particles. This results in significant time consumption for running these models. The code runs well for the first few million years, but maintaining an optimal resolution is crucial for efficient simulation.

Possible solutions to this issue include using more powerful computers, reducing resolution, spawning sink particles to combine gas particles in clumps, or selecting an appropriate range of initial conditions. As computation time grows exponentially, it becomes less helpful to continue running the code once it starts to slow down due to gas collapse. Reducing resolution would significantly speed up the simulations but would also discard many details, contrary to our scientific goals. Thus, selecting a fine range of

doi:10.6342/NTU202401221

initial conditions and setting up the corresponding resolution for the desired topics is the most important process in astronomical simulations.

Lastly, replacing clumpy gas particles with sink particles may be a potential solution for future work. In our model, we observed that turbulence energy decreases as density increases. It may be worth attempting to replace high-density particles with sink particles, such as stars, without affecting statistical results. In future work, these sink particles could represent Population III stars, incorporating appropriate initial mass functions and feedback models.

4.3 Is There a Relation Between the Characteristic Turbulence Mach Number and the Initial Conditions?

In this work, we aim to connect large-scale cosmological simulations with star-forming research in the early universe, providing insights for those who want to introduce driven turbulence into simulations. As mentioned in the introduction, turbulence sources can include stellar feedback, AGN feedback, and gravitational accretion. Assuming an environment where the first stars have not yet formed, we exclude any feedback in our simulation and focus on turbulence driven by gravitational accretion.

From Figure 3.14, we observed that the characteristic turbulence Mach number does not correlate with either the halo mass or the average matter density. This finding is intriguing, as it suggests that turbulence energy is independent of large-scale structure, indicating that the formation of the first stars is primarily influenced by the local environment.

Instead, we found that turbulence energy is more likely affected by local conditions,

doi:10.6342/NTU202401221

such as local density. Figures 3.16 and 3.17 show that turbulence energy increases from low to high density. However, once the local density reaches 10^{-22} g cm^{-3}, turbulence energy begins to decrease and becomes more scattered. In the densest regions, where the density reaches 10^{-22} g cm^{-3}, turbulence energy drops to the same level as the high-density region.

Figure 3.17 could serve as a reference for the strength of driven turbulence in cosmological simulations. For initial conditions in a mini-halo, driven turbulence around $\mathcal{M} = 2.20 \pm 1.67$ with the average density of 2.78×10^{-22} g cm^{-3} can be considered a plausible environment. For driven turbulence with $\mathcal{M} > 3.5$, the environment and results may not be realistic.

Overall, these results suggest that local environmental conditions, rather than large-scale structures, play a significant role in the formation and characteristics of turbulence in the early universe. This insight is crucial for accurately modeling star formation in the context of cosmological simulations.

doi:10.6342/NTU202401221

Chapter 5 Conclusion

In this thesis, we proposed a method to investigate the physical properties and the strength of turbulence in primordial star-forming clouds within mini-halos in the early universe at $z \approx 20$. The initial conditions were derived from the large-scale cosmological simulation IllustrisTNG. Using the cosmological hydrodynamic simulation code GIZMO with the Meshless-Finite-Mass method, we simulated mini-halos to reveal the intricate details within our models. To ensure that the models could evolve over a suitable period, we selected mini-halos with masses around 10^7 $M_\odot$.

We analyzed 26 models at $z \approx 19.40$, which had evolved over 7.9 million years from $z \approx 20$. Our findings indicate that the strength of turbulence is not sensitive to the halo mass or average matter density, suggesting that turbulence may not be strongly connected to the initial conditions. However, we observed that turbulence is correlated with the local density after collapse. In general, we found out that gas compression and vorticity are highly associated with the region with high density. Generally, gas compression and vorticity are highly associated with high-density regions. Molecular hydrogen plays a crucial role in the cooling process, especially in high-density areas. Additionally, we determined the Mach number to be $\mathcal{M} = 2.20 \pm 1.67$ in regions with a local gas density of 2.78×10^{-22} g cm^{-3}. In denser areas, the turbulence Mach number decreases but becomes more scattered.

doi:10.6342/NTU202401221

The estimation of turbulence strength can serve as a reference for simulations incorporating driven turbulence. However, caution is advised for initial conditions with densities greater than 10^{-22} g cm^{-3}, as these areas contain more complex structures. The theory of Population III star formation is still developing, with the mass of Pop. III stars potentially ranging from $25 \sim 100$ $M_\odot$ depending on the presence of turbulence (Tang & Chen, 2024, Sharda & Menon, 2024). Our results provide clues for constraining the predicted mass of Pop. III stars.

Future work will focus on analyzing the clumps within our models which are potential sites for Pop. III star formation. By gathering mass and turbulence information from these clumps, along with observational data from the James Webb Space Telescope (JWST), we aim to elucidate the relation between first star formation and mini-halo structures. This research will aid in predicting the initial mass function (IMF) of Pop. III stars.

doi:10.6342/NTU202401221

References

Abel, T., Bryan, G. L., & Norman, M. L. 1998, The Formation and Fragmentation of Primordial Molecular Clouds. https://arxiv.org/abs/astro-ph/9810215

Bromm, V. 2013, Reports on Progress in Physics, 76, 112901, doi: 10.1088/0034-4885/76/11/112901

Faucher-Giguère, C.-A., Lidz, A., Zaldarriaga, M., & Hernquist, L. 2009, ApJ, 703, 1416, doi: 10.1088/0004-637X/703/2/1416

Ferland, G. J., Chatzikos, M., Guzmán, F., et al. 2017, Rev. Mexicana Astron. Astrofis., 53, 385, doi: 10.48550/arXiv.1705.10877

Gaburov, E., & Nitadori, K. 2011, Monthly Notices of the Royal Astronomical Society, 414, 129, doi: 10.1111/j.1365-2966.2011.18313.x

Haardt, F., & Madau, P. 2012, ApJ, 746, 125, doi: 10.1088/0004-637X/746/2/125

Hirano, S., Hosokawa, T., Yoshida, N., et al. 2014, The Astrophysical Journal, 781, 60, doi: 10.1088/0004-637x/781/2/60

Hopkins, P. F. 2015, Monthly Notices of the Royal Astronomical Society, 450, 53–110, doi: 10.1093/mnras/stv195

doi:10.6342/NTU202401221

Hopkins, P. F., Wetzel, A., Kereš, D., et al. 2018, Monthly Notices of the Royal Astronomical Society, 480, 800–863, doi: 10.1093/mnras/sty1690

Hopkins, P. F., Wetzel, A., Wheeler, C., et al. 2022, Monthly Notices of the Royal Astronomical Society, 519, 3154–3181, doi: 10.1093/mnras/stac3489

Hosokawa, T., Hirano, S., Kuiper, R., et al. 2016, The Astrophysical Journal, 824, 119, doi: 10.3847/0004-637X/824/2/119

Ishigaki, M. N., Tominaga, N., Kobayashi, C., & Nomoto, K. 2018, The Astrophysical Journal, 857, 46, doi: 10.3847/1538-4357/aab3de

Ji, A. P., Curtis, S., Storm, N., et al. 2024, ApJ, 961, L41, doi: 10.3847/2041-8213/ad19c4

Katz, N., Weinberg, D. H., & Hernquist, L. 1996, ApJS, 105, 19, doi: 10.1086/192305

Klessen, R. S., & Glover, S. C. O. 2023, The first stars: formation, properties, and impact. https://arxiv.org/abs/2303.12500

Klessen, R. S., & Hennebelle, P. 2010, Astronomy and Astrophysics, 520, A17, doi: 10.1051/0004-6361/200913780

Monaghan, J. J. 1992, ARA&A, 30, 543, doi: 10.1146/annurev.aa.30.090192.002551

Omukai, K. 2001, ApJ, 546, 635, doi: 10.1086/318296

Omukai, K., & Palla, F. 2003, The Astrophysical Journal, 589, 677, doi: 10.1086/374810

O'Shea, B. W., & Norman, M. L. 2007, ApJ, 654, 66, doi: 10.1086/509250

doi:10.6342/NTU202401221

Pillepich, A., Springel, V., Nelson, D., et al. 2018, MNRAS, 473, 4077, doi: 10.1093/mnras/stx2656

Saslaw, W. C., & Zipoy, D. 1967, Nature, 216, 976, doi: 10.1038/216976a0

Sharda, P., & Menon, S. H. 2024, arXiv e-prints, arXiv:2405.18265, doi: 10.48550/arXiv.2405.18265

Skúladóttir, Á., Vanni, I., Salvadori, S., & Lucchesi, R. 2024, A&A, 681, A44, doi: 10.1051/0004-6361/202346231

Smith, B. D., Bryan, G. L., Glover, S. C. O., et al. 2017, MNRAS, 466, 2217, doi: 10.1093/mnras/stw3291

Springel, V. 2005, MNRAS, 364, 1105, doi: 10.1111/j.1365-2966.2005.09655.x

Tang, C.-Y., & Chen, K.-J. 2024, Clumpy Structures within the Turbulent Primordial Cloud. https://arxiv.org/abs/2303.00751

Umeda, H., & Nomoto, K. 2005, The Astrophysical Journal, 619, 427, doi: 10.1086/426097

Weinberger, R., Springel, V., Hernquist, L., et al. 2017, MNRAS, 465, 3291, doi: 10.1093/mnras/stw2944

Yoshida, N., Abel, T., Hernquist, L., & Sugiyama, N. 2003, The Astrophysical Journal, 592, 645–663, doi: 10.1086/375810

doi:10.6342/NTU202401221

doi:10.6342/NTU202401221

Appendix A — Convergence Test

Particle splitting is a required process when performing zoom-in simulation. However, since the process will spawn several particles, one needs to confirm the stability of the splitting algorithm before running the simulation. For example,

Here we show the results of convergence tests. We tested four resolutions for the same model sub-halo 27075, with the resolutions of $0.1, 1, 10$, and $100 M_{\odot}$ for the gas particles, respectively.

A.1 Density Rendering Plots

Figure A.1 shows the density rendering in different resolutions while maintaining the same center, region, and rendering scale. The top-left panel From the figure, we notice the dense area in the four parts is nearly at the same region, which means the simulation results are consistent even if we change the resolutions.

Most importantly, the structures and details in the simulations are getting clearer when the resolution is better. This shows the necessity that we need to perform the particle splitting methods to get them and further analyze the simulation area.

doi:10.6342/NTU202401221

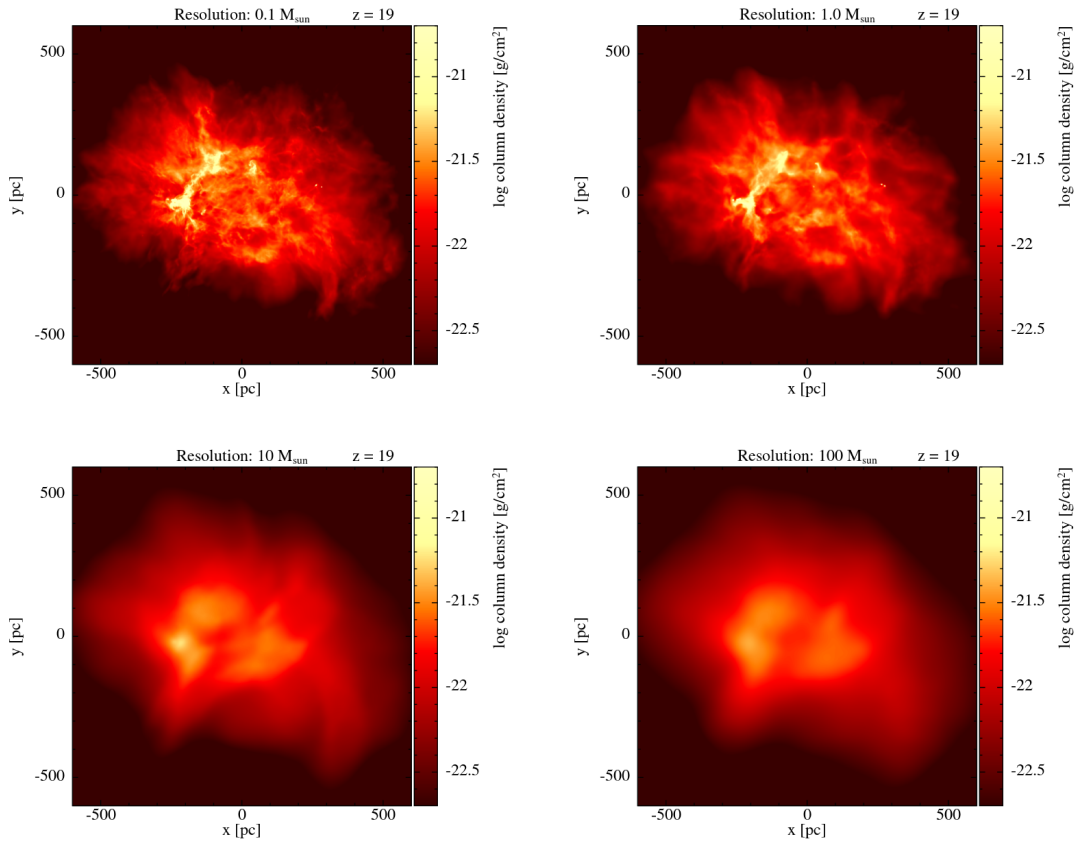

Figure A.1: Density rendering plots of different resolutions. Top left: 0.1 $M_{\odot}$. Top right: 1.0 $M_{\odot}$. Bottom left: 10 $M_{\odot}$. Bottom right: 100 $M_{\odot}$

doi:10.6342/NTU202401221

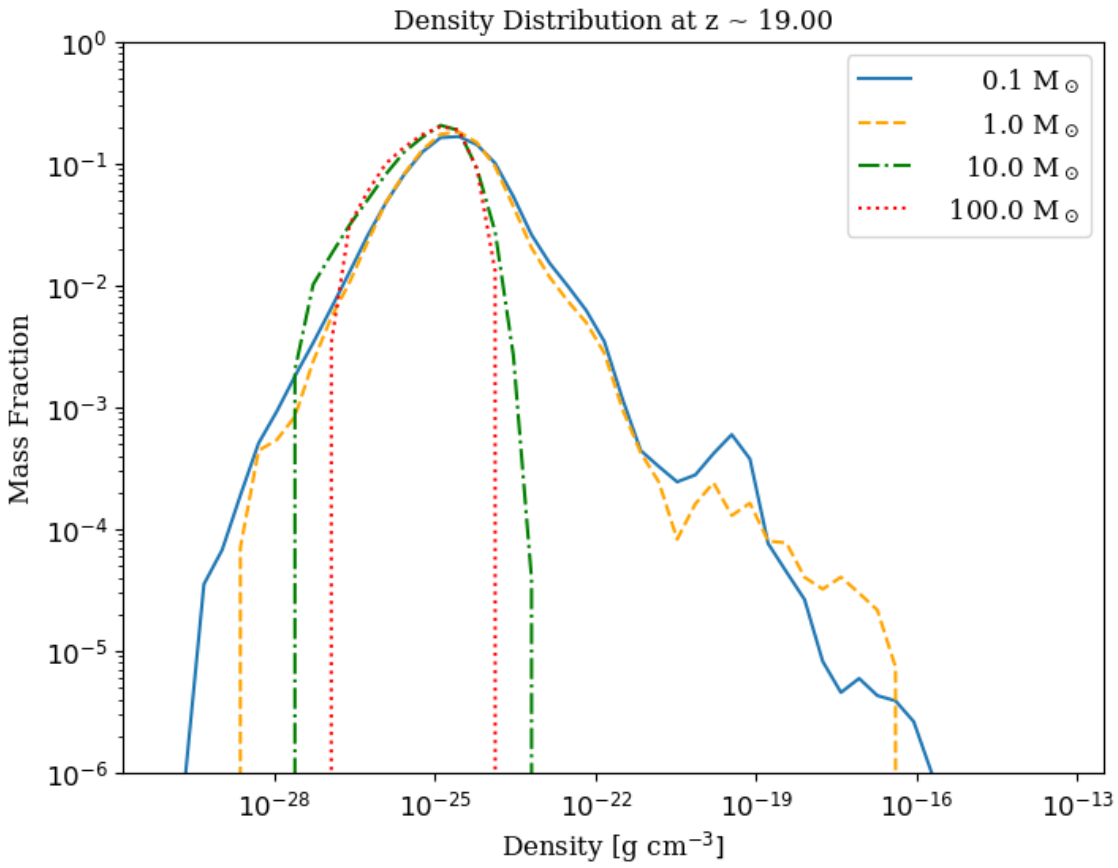

Figure A.2: Density distribution of different resolutions.

A.2 Density Distribution

Figure A.2 shows the results of density distribution. From the figure, we can notice that the solid blue line represents the highest resolution, $0.1M_{\odot}$, and has the most smoothed curve. When the resolution goes low, the curve becomes disconnected and varies a lot.

For the high-density end, although the densest result is obtained in the second-lowest resolution line, this result could be biased due to the low resolution. In this case, the density can't be resolved fine since every particle carries too much mass. Once any two particles are getting too close, it is easy to obtain the high-density results. This can also be noticed from the fact there are lots of gaps in the low-resolution three curves, which means the code faces this issue frequently when the particles are not well-distributed.

doi:10.6342/NTU202401221

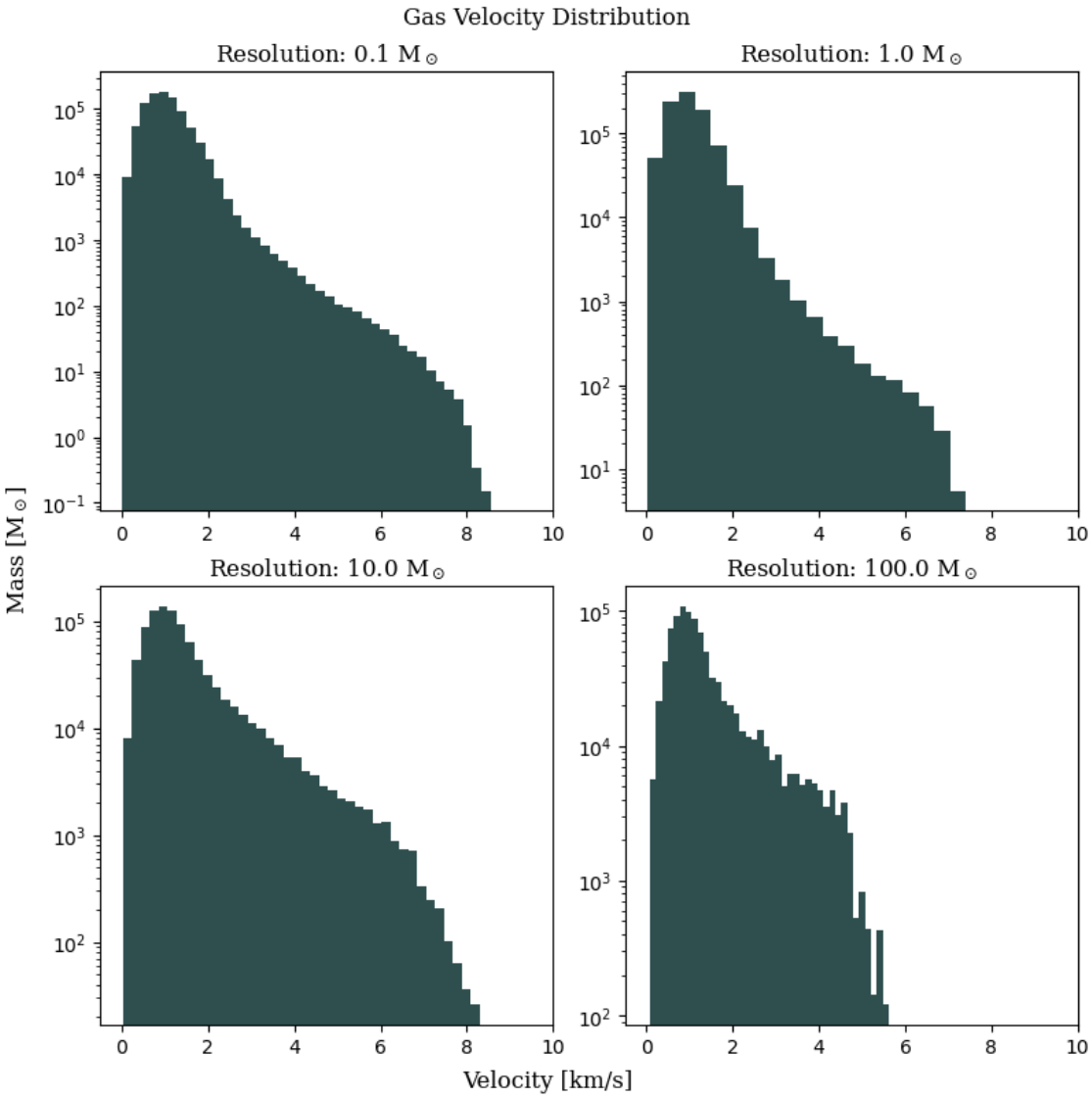

Figure A.3: Velocity distribution

As a result, the lines with $0.1M_{\odot}$ and $1M_{\odot}$ resolutions show stability in the high-density area. Also, all resolutions agree well with the density distribution around $\sim 10^{-25}$ g cm^{-3} where most of the particles exist.

A.3 Velocity Distribution

Figure A.3 shows the velocity distribution of different resolutions. In the figure, we notice the shapes of the distribution are similar across all resolutions. This shows

doi:10.6342/NTU202401221

the consistency in our simulations. Also, with the higher resolution, a larger value of maximum velocity can be obtained. This tells us that we can better resolve the velocity field when increases the resolution, and is crucial for us to analyze the turbulent area.

doi:10.6342/NTU202401221